



OPEN

The translation factor eIF4E is a key mediator of doxorubicin resistance: insights from a triple-negative breast cancer model

Héctor Frayde-Gómez^{1,2}, Brenda Chimal-Vega^{1,2}, Angel Pulido-Capiz^{1,2},
 Andrea Muñoz-Ayala^{1,2}, Octavio Galindo-Hernández^{1,2}, José Luis Vique-Sánchez^{2,3},
 Ana Gabriela Leija-Montoya^{2,3}, Raúl Díaz-Molina⁴, Pablo A. Madero-Ayala⁵,
 Marco A. Ramos-Ibarra⁵ & Victor García-González^{1,2}✉

Triple-negative breast cancer (TNBC) tumors are highly aggressive and typically associated with poor prognosis due to limited therapeutic options and significant chemoresistance. This study investigated the role of the translation initiation factor eIF4E in doxorubicin (Dox) resistance using a novel TNBC model. A doxorubicin-resistant cell variant, MDA_R ($IC_{50}=1.8\text{ }\mu\text{M}$), was derived from MDA-MB-231 cells ($IC_{50}=0.6\text{ }\mu\text{M}$) following prolonged exposure to Dox at its IC_{25} concentration. Compared to the parental line, MDA_R cells exhibited enhanced migration, invasion, and drug efflux capabilities. Dox treatment sustained the phosphorylation of eIF4E at Ser209 (eIF4E-p^{Ser209}), which promoted activation of the VEGF pathway and secretion of matrix metalloproteinase-9 (MMP-9). This dysregulated phosphorylation correlated with increased expression of the ABCB1 drug transporter, as confirmed by treatment with the eIF4E inhibitor 4E1RCat. In silico molecular docking and dynamics simulations further demonstrated the Dox-binding affinity of ABCB1. Moreover, at higher Dox concentrations, MDA_R cells showed elevated Nrf2 activation. Conversely, eIF4E knockdown via siRNA reduced both chemoresistance and Nrf2 expression. These findings suggest that Dox resistance enhances cellular invasiveness through an eIF4E-dependent mechanism involving ABCB1 and Nrf2, both of which are overexpressed in TNBC transcriptomic datasets, highlighting their potential clinical relevance.

Keywords Triple-negative breast cancer, EIF4E, Chemoresistance, ABCB1, Doxorubicin

Breast cancer (BC) is the most frequently diagnosed malignancy and a leading cause of cancer-related mortality in women worldwide. According to 2022 data from the International Agency for Research on Cancer (IARC), breast cancer accounted for 2.3 million new cases and over 8 million prevalent cases worldwide, with a mortality rate ranging from 9 to 13%^{1,2}.

BC is classified into four subtypes: Luminal A, Luminal B, human epidermal growth factor receptor 2 (HER-2)-positive, and triple-negative breast cancer (TNBC). This classification is based on immunohistochemistry detection of estrogen receptor alpha (ER α), progesterone receptor (PR), HER-2, and the proliferation biomarker, Ki-67^{1,3}. Tumors with triple-negative features (TNBC: ER α -, PR-, and HER-2-) are highly aggressive. In this regard, patients who develop metastatic TNBC typically have a short life expectancy, with relapse occurring in less than three years and overall survival not exceeding five years post-diagnosis^{4,5}. During tumor progression, several processes, such as cellular invasion, metastasis, angiogenesis⁶, and chemoresistance⁷, are critical for cancer evolution and clinical outcome.

¹Departamento de Bioquímica, Facultad de Medicina Mexicali, Universidad Autónoma de Baja California, Mexicali, California 21000, México. ²Centro de Innovación e Investigación en Salud, CIIS, Universidad Autónoma de Baja California, Mexicali 21000, México. ³Centro de Ciencias de la Salud Mexicali, Universidad Autónoma de Baja California, Mexicali 21000, México. ⁴Departamento de Educación e Investigación, Centro Cívico y Comercial, Servicios de Salud del Instituto Mexicano del Seguro Social para el Bienestar (IMSS-BIENESTAR), Av. Pioneros No. 1005, Palacio Federal, 3er piso, Mexicali 21000, Baja California, México. ⁵Grupo de Investigación en Biotecnología y Biociencias, Facultad de Ciencias Químicas e Ingeniería, Universidad Autónoma de Baja California, Tijuana 22390, México. ✉email: vgarcia62@uabc.edu.mx

Chemotherapy is the standard clinical treatment for TNBC. However, chemoresistance is the main obstacle to therapeutic success, especially in metastatic tumors, wherein chemotherapy failure accounts for up to 80–90%^{8–10}. Chemoresistance mechanisms in TNBC are multifactorial and based on a complex interaction between the tumor microenvironment, the expression of transporters for drug efflux, alteration in signaling pathways such as PI3K/Akt/mTOR^{11–13}, and overexpression of targets such as vascular endothelial growth factor (VEGF)¹³. These mechanisms regulate the translational modulator complex eukaryotic initiation factor 4 F (eIF4F)¹⁴.

Translational control occurs predominantly at the initiation stage, wherein the eIF4F complex plays a key role. eIF4F is a heterotrimeric complex composed of protein eukaryotic initiation factor 4E (eIF4E), which binds the 7-methylguanosine (m7G) cap; eukaryotic initiation factor 4 A (eIF4A), which unwinds secondary structures on 5' untranslated regions of the mRNA (RNA G-quadruplex), and the scaffold protein eukaryotic initiation factor 4G (eIF4G). eIF4E has been associated with cancer hallmarks such as invasion capability, impacting metastasis development¹⁵, and a dependent process on protein translation initiation¹⁶.

eIF4E represents the limiting factor in the eIF4F complex activity; the primary eIF4E function is to mediate ribosome recruitment on the specific mRNA to begin protein synthesis¹⁷. The formation of an active initiation complex containing eIF4G is hindered when eIF4E is coupled to the eIF4E-binding proteins 1, 2, and 3 (4EBPs), which inhibit cap-dependent translation in their hypophosphorylated state. Their phosphorylation status, regulated by the rapamycin (mTOR) pathway's mammalian target determines their binding affinity to eIF4E¹⁸. This process is crucial for activating the translation machinery regulated upstream by the mTOR pathway¹⁸.

The relative abundance of eIF4G and the regulation of 4EBPs influence cap-dependent translation. Targeting eIF4E is a promising strategy to suppress translation in cancer cells using small interfering RNA (siRNA) or small molecules. 4E1RCat, for example, inhibits eIF4E activity and has shown efficacy in hepatocarcinoma and melanoma cells¹⁹.

eIF4E is overexpressed in several cancer types^{20–22}. Its phosphorylation at Ser209 (eIF4E-p^{Ser209}), catalyzed by MAPK-interacting kinases (Mnks)²³, promotes the translation of genes involved in tumorigenesis. However, its role in chemoresistance remains to be fully elucidated. Components of the eIF4F complex may also participate in the translation of nuclear factor erythroid 2-related factor 2 (Nrf2)²⁴, a transcription factor involved in stress responses and detoxification^{25,26}, functions possibly linked to chemoresistance.

Nrf2 is the master regulator of redox homeostasis and is activated under oxidative stress²⁷. Its activation contributes to cancer progression and metastasis²⁸ and may enhance drug efflux²⁹. Upon activation, Nrf2 dissociates from KEAP1, translocates to the nucleus, and heterodimerizes with Maf proteins to promote the transcription of genes with antioxidant response elements (AREs), including ATP-binding cassette (ABC) transporters³⁰.

ABC subfamily B member 1 (ABCB1) is implicated in the processing of anthracyclines³¹ and in the development of chemoresistance³². An Nrf2-dependent regulation of ABCB1, potentially involving eIF4E, has been proposed^{33,34}. ABCB1 overexpression correlates with reduced survival, higher relapse rates, and poor prognosis³⁵.

Elucidating the role of eIF4E regulation in a doxorubicin-resistant TNBC model could enhance our understanding of the chemoresistance process, particularly those associated with increased migration and invasion, key factors in TNBC malignancy. At a cellular level, breast cancer is heterogeneous, with multiple subpopulations of breast tumor cells³⁶. Specifically, the MDA-MB-231 cell line is considered a mesenchymal stem-like model, making it suitable for studying TNBC. Therefore, we developed a novel strategy using the cell viability inhibitory concentration 25 (IC₂₅) of the TNBC MDA-MB-231 cells (denominated MDA_N) to generate a chemoresistant variant named MDA_R. Critically, this MDA_R variant showed an inhibitory concentration 50 (IC₅₀) value three times higher than MDA_N and has optimized management of doxorubicin coupled with the high capability for cellular migration and invasion. Mechanisms such as ABCB1 expression and Nrf2 activation, potentially modulated by eIF4E, may underlie this chemoresistance. These findings are supported by eIF4E silencing via siRNA and inhibition by 4E1RCat, suggesting that the eIF4E/Nrf2/ABCB1 axis may play a central role in doxorubicin resistance in TNBC.

Results

Generation of doxorubicin-resistant MDA-MB-231 cells

To generate doxorubicin (Dox)-resistant cellular models, we established two protocols based on the IC₂₅ (14 months or 7 cycles) and IC₅₀ (Sup. Figure 1). Considering the high effectiveness of dox, we employed an IC₂₅ strategy (0.3 μ M) to generate a chemoresistant variant referred to as MDA_R (Fig. 1A). Viability assays assessed MDA_R chemoresistance at increasing concentrations of dox (0–6.4 μ M), and the IC₅₀ value was subsequently determined. Notably, the MDA_R cells (IC₅₀ = 1.883 μ M) exhibited significant doxorubicin resistance, displaying an IC₅₀ value three times higher than MDA_N cells (IC₅₀ = 0.619 μ M) under the same conditions (Fig. 1B–C). This phenotype may be explained by the cellular processes associated with drug metabolism. MDA_R variant cells must develop dox-induced mechanisms that favor drug resistance, decreased intracellular accumulation, or enhanced efflux of doxorubicin.

Chemoresistance is associated with optimized doxorubicin management in MDA_R cells

To investigate the mechanisms underlying chemoresistance, we analyzed cellular handling of doxorubicin (Dox), by quantifying its concentration in the culture supernatant and through flow cytometry assays. This strategy leveraged the intrinsic fluorescence of Dox. Then, we assessed extracellular Dox levels to characterize drug management related to either increased efflux or decreased intracellular accumulation (Fig. 2A, B). Cell cultures were treated with increasing concentrations of Dox (0–3.2 μ M) for 24 h (Fig. 2A) and 48 h (Fig. 2B) to evaluate dose- and time-dependent responses. Supernatants were collected and analyzed by spectrofluorometry using a previously established standard curve. The data revealed significantly higher Dox concentrations in

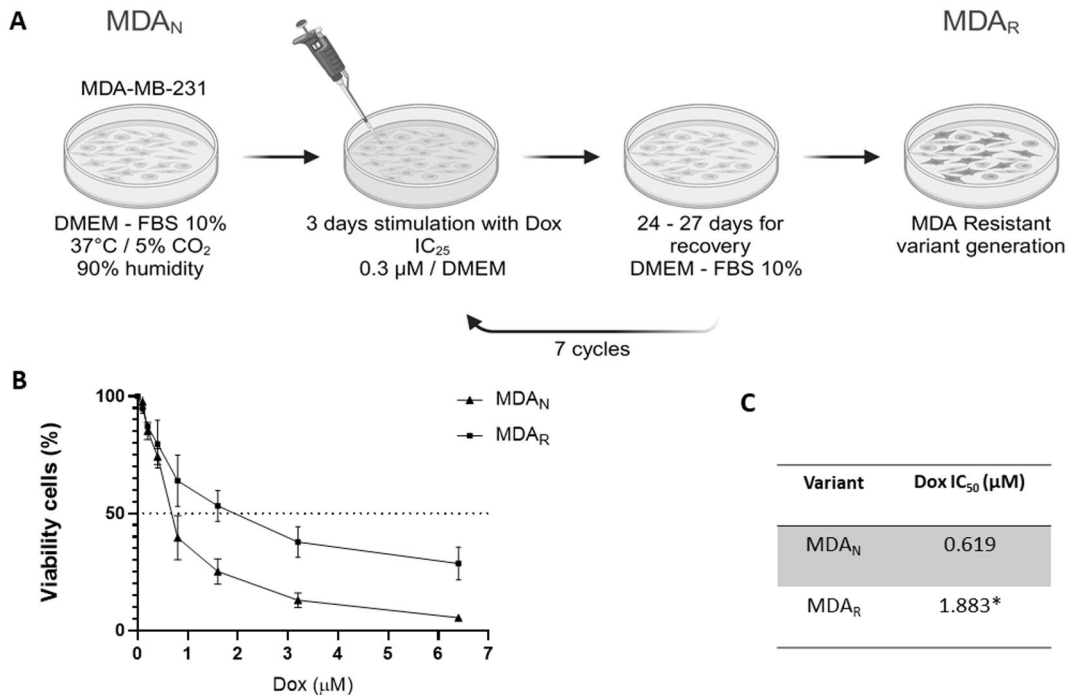


Fig. 1. Generation of chemoresistance phenotype using doxorubicin IC₂₅ (0.3 μM). (A) General scheme of the protocol for chemoresistance generation. (B) Dose-response curve under treatment with dox (0–6.4 μM) in MDA_N and MDA_R variant cells at 48 h treatment. (C) IC₅₀ values for the MDA_N and MDA_R cell variants, assays corresponding to three biological replicates (x ± S.D.). The mean values are presented ($n = 3$, mean ± SD); data were statistically analyzed using one-way ANOVA and Newman–Keuls's multiple comparison test, * $p < 0.05$. (1) FBS: Fetal bovine serum; (2) MDA_N: MDA native 3; MDA_R: MDA resistant variant.

supernatant media of MDA_R cells at 24 h from dox concentration 1.6 to 3.2 μM regarding MDA_N (Fig. 2A). For 48 h of treatment, the difference was significant from dox 1.6 μM (Fig. 2B). In both conditions, 24 h and 48 h, cell cultures of MDA_R maintained higher dox concentrations in supernatant media compared to MDA_N cells, suggesting enhanced drug efflux or reduced uptake.

On the other hand, under increasing concentrations of Dox (0–1.6 μM) for 24 h, MDA_N cells were analyzed by flow cytometry to evaluate their capacity for drug efflux, as cells unable to export Dox would retain it and exhibit fluorescence. A progressive increase in fluorescence was observed up to a concentration of 0.8 μM in both MDA_N and MDA_R cells (Fig. 2C). However, at higher concentrations (0.8–1.6 μM), a second population of MDA_N cells emerged in the region of lower fluorescence intensity, compared to MDA_R. This shift is likely associated with decreased cell viability.

To further evaluate Dox internalization, we measured the mean fluorescence intensity (MFI), which reflects intracellular drug content independently of the number of fluorescent cells.

As shown in the plots, although the MDA_N population included fewer viable cells, these exhibited higher fluorescence intensity than MDA_R cells, indicating greater intracellular accumulation of Dox. Conversely, in the MDA_R variant, fluorescence intensity decreased as the number of viable cells increased (Fig. 2C). These findings suggest that adaptive mechanisms in MDA_R cells may regulate intracellular Dox levels by enhancing drug efflux, thus contributing to sustained chemoresistance in association with cancer-related hallmarks.

Chemoresistance impact on cellular migration

A key characteristic of triple-negative breast cancer (TNBC) and chemoresistant cells is their high migratory capacity. To evaluate this, cell migration was assessed in MDA_N and MDA_R variants under increasing concentrations of doxorubicin (0.05–3.2 μM). Representative images of the migration assay for both cell lines are shown in Fig. 3A.

Cells cultured in unsupplemented DMEM were used as a negative control, while cells stimulated with DMEM supplemented with 10% fetal bovine serum (FBS) served as a positive control. Treatments with increasing Dox concentrations (0.05–3.2 μM) were performed under positive control conditions for both variants.

In MDA_N cells, the positive control induced a 2.8-fold increase in cell migration, and exposure to 0.05 μM Dox further enhanced migration to 3.12-fold over the negative control, as determined by densitometric analysis (Fig. 3B). This stimulatory effect was maintained up to 0.4 μM Dox. However, a significant dose-dependent decrease in migration was observed at Dox concentrations ranging from 0.8 to 3.2 μM.

In contrast, MDA_R cells displayed a different response: low Dox concentrations (0.05–0.8 μM) led to an increase in migration compared to the negative control (5.0 and 5.23-fold respectively), and a reduction in migration was only evident at higher concentrations (1.6 and 3.2 μM) (Fig. 3B).

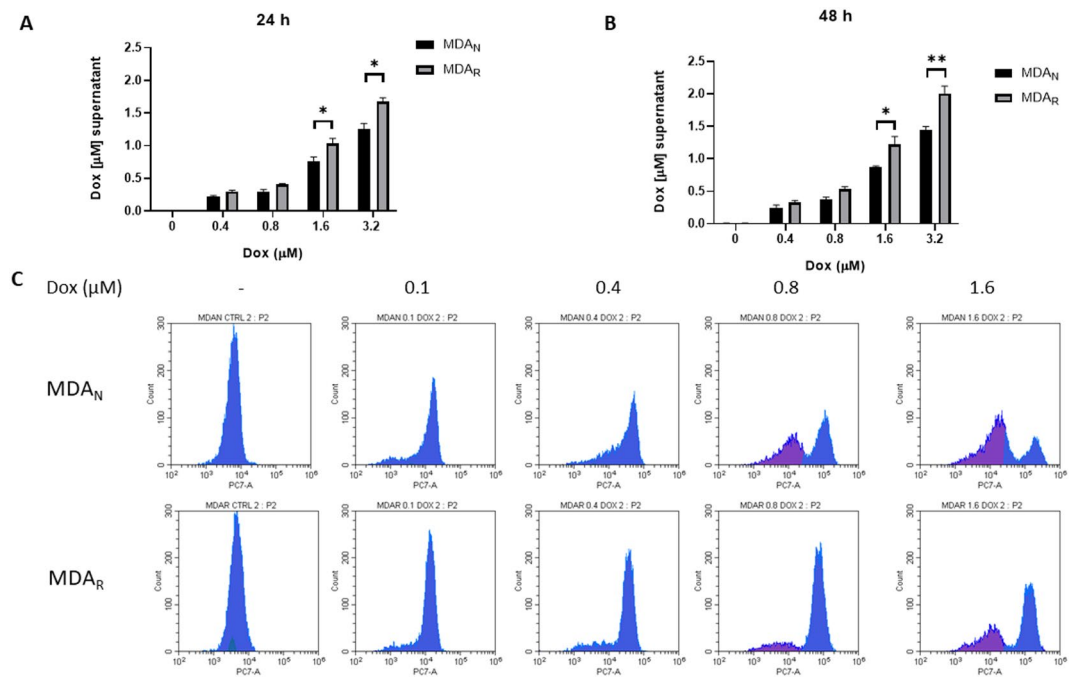


Fig. 2. Doxorubicin chemoresistance in MDA-MB-231 cells is associated with an optimized intracellular dox excretion. Doxorubicin quantification in supernatant media at 24 (A) and 48 h (B) stimuli (0–3.2 μM) on MDA_N and MDA_R cells; values were determined with three replicates, represented as mean and standard deviation ($n=3$, $\bar{X} \pm \text{S.D.}$). Data were statistically analyzed using one-way ANOVA and Newman–Keul's multiple comparison test, * represents a p value < 0.05 , ** represents a p value < 0.01 . Dox emission values of fluorescence at 560 nm were reported. C) Cytometry assays were performed to evaluate the effects of dox on MDA_N and MDA_R cellular variants under 24 h of treatment; for analysis, mean fluorescence intensity (MFI) was evaluated.

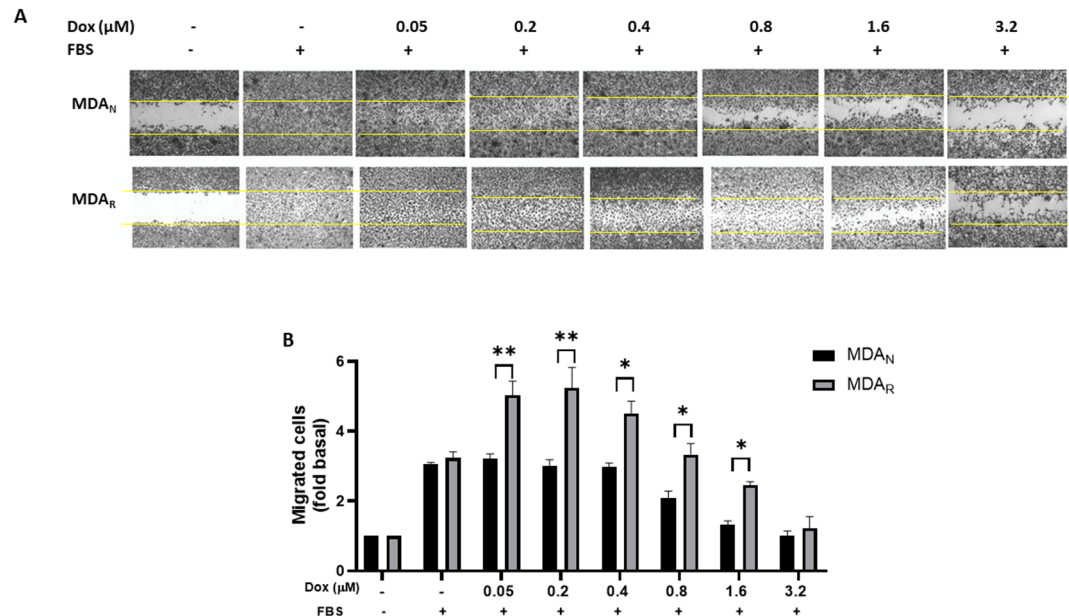


Fig. 3. Low doxorubicin concentrations promote cellular migration in MDA_R cells. (A) Representative images of wound-healing assays under treatment with increasing dox concentrations (0.05–3.2 μM) in MDA_N and MDA_R cell cultures. (B) Densitometric analysis of migration assays in the MDA_N and MDA_R variants. Results showed three biological replicates' mean and standard deviation ($n=3$, $\bar{X} \pm \text{S.D.}$). To evaluate this process, DMEM plus 10% fetal bovine serum (FBS) was used as a positive control, and a non-supplemented DMEM medium was used as a negative control. Data were statistically analyzed using one-way ANOVA, and Newman–Keul's multiple comparison test * represents a p value < 0.05 , ** represents a p value < 0.01 .

Based on the results, MDA_R cells exhibited a higher migratory capacity compared to MDA_N cells. Notably, this increase was more pronounced at low concentrations of doxorubicin (0.05–0.2 μ M), potentially reflecting adaptive mechanisms related to drug metabolism. This behavior is consistent with the observed IC₅₀ values: 1.88 μ M for MDA_R and 0.619 μ M for MDA_N, indicating greater sensitivity of the MDA_N variant to Dox treatment. These findings suggest that specific signaling pathways may regulate chemoresistance, with mechanisms such as protein translation initiation playing a critical role. Indeed, components of the eukaryotic initiation factor 4 F (eIF4F) complex have been identified as key modulators in the acquisition of chemoresistance³⁷.

Chemoresistance is associated with eIF4E dysregulation

We focused on modulating the eIF4E factor by evaluating its total expression, the phosphorylated form eIF4E-p^{Ser-209} mediated by MNK activation and associated regulatory mechanisms. For this characterization, Dox treatments were used under specific increasing doses (0–1.6.6 μ M) for 48 h, according to previous results.

As shown in Fig. 4A, the expression levels of total eIF4E and its active phosphorylated form eIF4E-p^{Ser-209}, both of which are associated with cancer aggressiveness¹⁶, were examined. Under the doxorubicin dose-dependent treatment (0–1.6.6 μ M), the expression of eIF4E was diminished in the MDA_N variant. However, its levels were constant in the MDA_R variant, even at the highest Dox concentration tested (1.6 μ M), which approximates the IC₅₀ for this variant (Fig. 4A, B). This differential expression pattern may be linked to chemoresistance, altered Dox handling, and increased migratory capacity. To explain these phenomena, while a diminution of phosphorylation (eIF4E-p^{Ser-209}) dependent on the doxorubicin dose was registered in the MDA_N variant, the eIF4E-p^{Ser-209} levels were maintained constant in the MDA_R variant. Notably, a slight increase in eIF4E-p^{Ser-209} was observed in MDA_R cells at 1.6 μ M Dox (Fig. 4A, C), suggesting sustained eIF4E activation under chemotherapeutic stress.

In addition, a key regulatory mechanism of eIF4E activity is the role of 4EBPs¹⁷, whose phosphorylation induced by the Akt/mTORC1 pathway blocks the binding to eIF4E. In the evaluation of the phosphorylation levels 4EBP1/2/3, revealed a dose-dependent decrease in phosphorylation in MDA_N cells as Dox concentration increased (Fig. 4A, D). In contrast, in the MDA_R variant, an increase in the phosphorylation of these regulatory proteins was registered (Fig. 4A, D). The evidence suggests the conservation of mechanisms such as the Akt/mTORC1 despite the treatment with high dox concentrations, increasing the 4EBP1/2/3 phosphorylation in the MDA_R variant.

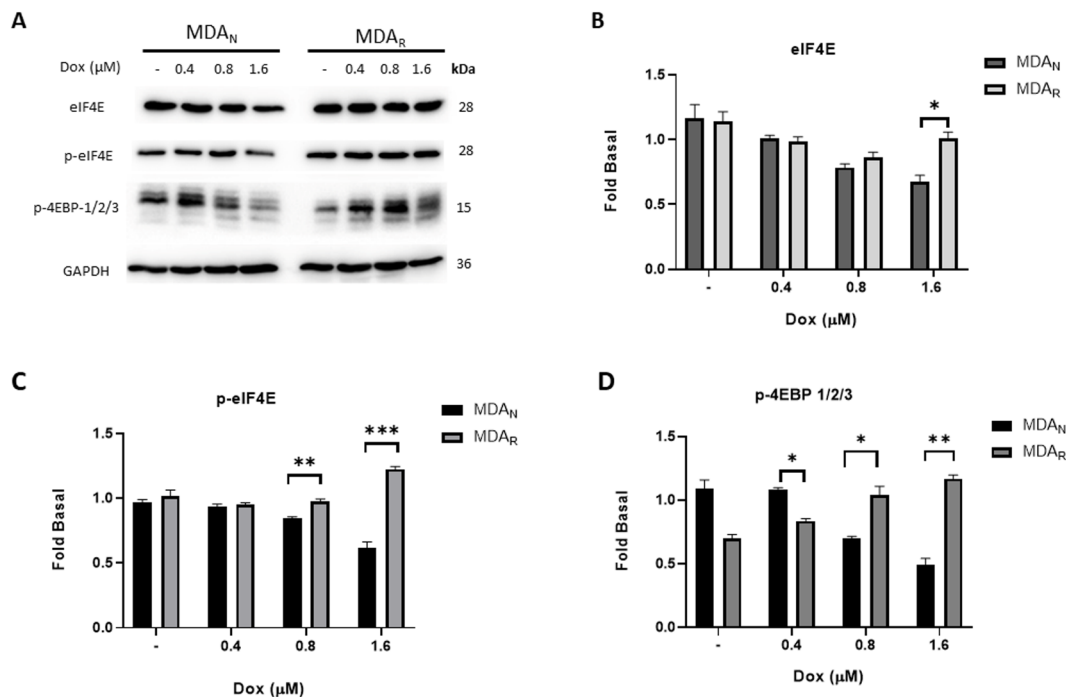


Fig. 4. In the chemoresistant variant MDA_R, eIF4E's higher expression and activity are registered under high dox concentrations. **A)** Characterization of targets eIF4E, eIF4E-p^{Ser-209}, and p-4EBP1/2/3 on MDA_N and MDA_R cellular variants under increasing dox range (0–1.6.6 μ M) treatment. Densitometry determinations of eIF4E (**B**) and eIF4E-p^{Ser-209} (**C**), respectively. **D)** Detection of phosphorylation levels of eIF4E activity regulator 4E-BP1/2/3 under dox range concentration (0–1.6.6 μ M); densitometry analysis is shown using GAPDH as the control. Three replicates data were statistically analyzed using one-way ANOVA, and Newman–Keuls's multiple comparison test * represents a p -value < 0.05 , ** represents a p -value < 0.01 , and *** represents a p -value < 0.001 .

elf4E pathway, a critical factor for chemoresistance

Furthermore, we assessed the expression of the eIF4A and eIF4G factors in the MDA_N and MDA_R cells under treatment with increasing concentrations of Dox (0–1.6.6 μ M) (Fig. 5A, B, C). In MDA_R cells, eIF4G expression increased at 0.4 and 0.8 μ M Dox, but decreased at 1.6 μ M (Fig. 5A, B). To examine the formation of the eIF4F complex, eIF4E was immunoprecipitated from whole-cell lysates, and associated eIF4G and eIF4A were detected (Sup. Figure 2 A). Notably, eIF4G recruitment differed between MDA_N and MDA_R variants, indicating Dox-induced dynamic regulation of eIF4F complex assembly.

Free eIF4E and its phosphorylated form eIF4E-p^{Ser-209} are implicated in cancer hallmarks such as cell death resistance and angiogenesis, by promoting the translation of targets such as Bcl-2 and VEGF, respectively¹⁶. Critically, in melanoma patients with VEGF overexpression, the VEGF/VEGFR axis can be associated with higher levels of tumor invasion and a poor response to therapy³⁸. However, this effect has not yet been clearly described in breast cancer models.

Our results demonstrated a direct association in MDA_R cells between sustained eIF4E phosphorylation (Fig. 4A, C) and VEGF expression (Fig. 5D, E), even under Dox treatment at high concentrations (1.6 μ M), a dose close to the IC₅₀ (1.88 μ M). In contrast, MDA_N cells exhibited the opposite response: VEGF expression was downregulated in parallel with reduced eIF4E-p^{Ser-209} phosphorylation, particularly at 1.6 μ M Dox (Fig. 5D, E).

This phenomenon could contribute to a differential response in processes that support the oncogenic pathways, such as cell invasion, and explain the effects of chemoresistance.

The secretion of matrix metalloproteinase-9 (MMP-9) is closely associated with enhanced migratory and invasive capabilities in cancer cells³⁹. To assess this, we evaluated MMP-9 activity in the extracellular medium of both cell variants under high Dox concentrations (1.6 μ M). The results showed elevated MMP-9 activity in MDA_R cells. In contrast, MMP-9 activity was reduced in MDA_N cells treated under the same conditions (Fig. 5F, G).

This differential response aligns with the regulation of the translational factor eIF4E and is consistent with the observed variations in invasive behavior. Notably, increasing Dox concentrations (0–1.6 μ M) significantly impaired the invasive capacity of MDA_N cells, whereas MDA_R cells retained their invasive potential (Fig. 5H).

Moreover, invasion activity in MDA_R cells was still detected at the highest Dox concentrations (0.8–1.6 μ M), correlating with sustained MMP-9 activity (Fig. 5I). These findings highlight a key phenotypic difference in the chemoresistant MDA_R variant, supporting the notion that invasive properties persist despite exposure to cytotoxic doses of Dox.

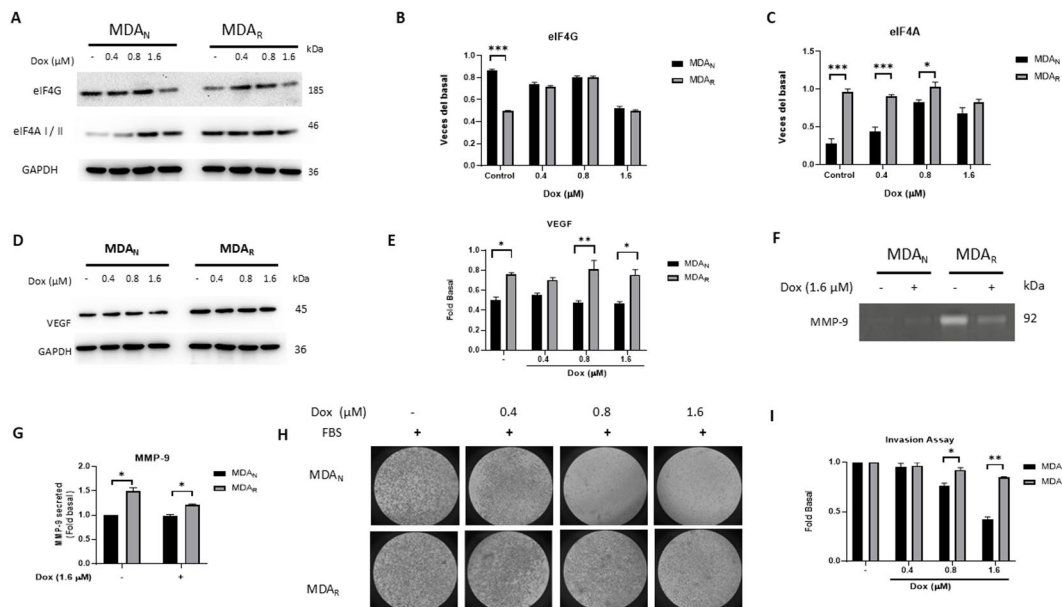


Fig. 5. eIF4E pathway, a critical factor for chemoresistance. MDA_N and MDA_R cells were stimulated with dox increasing concentrations (0–1.6.6 μ M) at 48 h treatment; (A) Western blot analysis of the scaffold protein eIF4G and helicase protein eIF4A and their densitometric analysis (B) and (C) respectively. (D) Western blot of VEGF expression in both variants, GAPDH was used as a loading control. (E) Densitometry analysis of VEGF. (F) Metalloproteinase-9 activity evaluated by zymography and respective densitometric analysis (G); results showed the mean and standard deviation ($X \pm S.D.$) of three biological replicates. To assess this process, MDA_N control sample was used as control. (H) Representative images of cell invasion experiments in MDA_N and MDA_R cells under treatment with increasing dox concentrations (0–1.6.6 μ M) and concomitant FBS (10%). (I) Densitometric analysis of invasion assays in the MDA_N and MDA_R variant. Results showed three biological replicates' mean and standard deviation ($n = 3, X \pm S.D.$). To evaluate this process, DMEM plus 10% fetal bovine serum (FBS) was used as a positive control. Data were statistically analyzed using one-way ANOVA and Newman-Keuls's multiple comparison test, * represents a p value < 0.05 ** represents a p value < 0.01 .

The role of ABC transporters in doxorubicin chemoresistance

We evaluated the implication of the ABC transporters as a determinant of chemoresistance. In the first strategy, we selected representative transporters of this superfamily. We established the conditions for ABCC1 and ABCB1 characterization through qPCR. Under basal conditions, ABCC1 expression was slightly higher in MDA_R cells compared to MDA_N cells (Fig. 6A). Upon Dox treatment (0–1.6 μ M), a modulation in ABCC1 expression was observed, suggesting a downregulation in MDA_R cells (Fig. 6A). However, significant differences were not detected between MDA_R and MDA_N at any Dox concentration tested (0–1.6 μ M). These responses may correspond with other compensatory mechanisms to maintain cell viability in MDA_R cells.

Under the same Dox treatment (0–1.6.6 μ M), we reported a crucial cell response, the ABCB1 overexpression in both cellular variants, which was dependent on Dox concentrations (Fig. 6B). Notably, this effect was more pronounced in the MDA_R variant. Based on the results, ABCB1 expression was significantly upregulated in MDA_R cells starting from 0.4 μ M Dox, with a substantial increase observed at 1.6 μ M (Fig. 6B). In MDA_N cells, ABCB1 expression also increased in a dose-dependent manner, although to a lesser extent. This response contrasts with ABCC1, whose expression remained marginally higher in MDA_R cells only under basal conditions and was not significantly modulated by Dox treatment. Data suggested ABCB1 could be the determining transporter in doxorubicin chemoresistance, which has been described in other types of cancer⁴⁰.

In this context, molecular docking simulations further support the involvement of ABCB1 in doxorubicin transport (Fig. 6C, D). Doxorubicin was found to dock within the transmembrane domains 1 and 2 (TMD1/2) of ABCB1, interacting specifically with residues Phe343, Gln347, Glu875, and Gln946, which are known to be critical for substrate recognition and stabilization. The calculated S-score of –8.977 indicates a stable and energetically favorable binding conformation. Key interactions included multiple hydrogen bonds, particularly with Gln195, Gln347, and Glu875, as well as hydrophobic contacts involving aromatic residues such as Phe343, positioning the anthracycline ring within the central substrate-binding cavity of ABCB1.

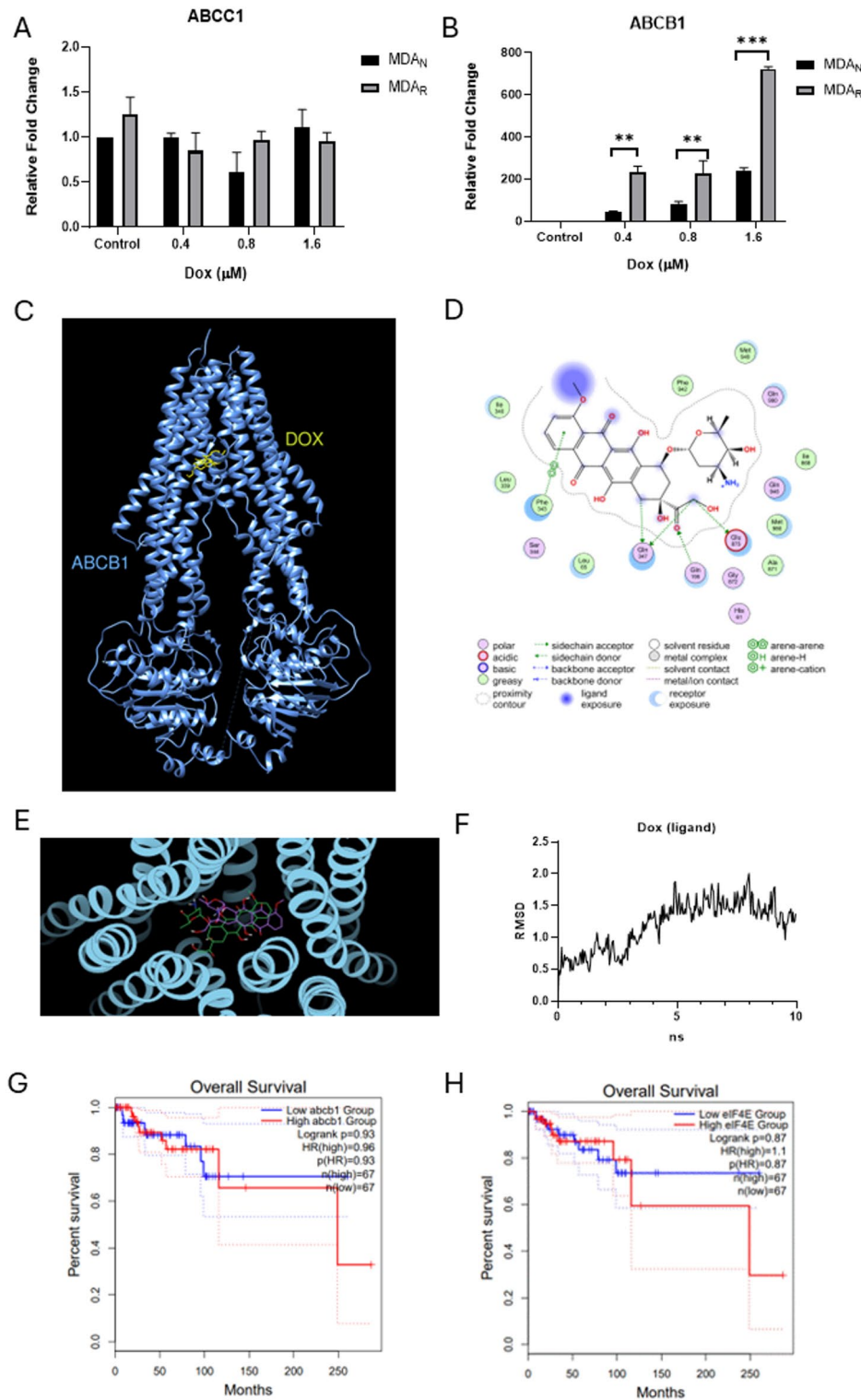
For the validation of the docking results, Rhodamine 123, a well-characterized ABCB1 substrate, was used as a control. Molecular docking simulations revealed that Rhodamine 123 binds within the transmembrane substrate-binding cavity of ABCB1, engaging several key residues including Ile340, Gln990, Gln347, Leu65 and Phe983 (Sup. Figure 3). Notably, several of these residues, particularly Glu875, Gln990 and Phe343 also participate in the binding of doxorubicin, indicating a partial overlap in their binding pockets. However, doxorubicin interacts with a broader and more intricate network of residues, including Gln946, Met986 and Gln195 which are absent in the Rhodamine 123 binding profile. These additional contacts likely contribute to the higher binding affinity and enhanced conformational stability observed for doxorubicin within ABCB1. The partial overlap in binding sites, along with differences in interaction profiles, suggests that doxorubicin and Rhodamine 123 share a common substrate recognition domain within ABCB1, reinforcing the transporter's role in Dox efflux (Fig. 6C).

In a complementary way, we conducted a docking using AutoDock Vina to evaluate further the binding affinities and interaction profiles of doxorubicin and Rhodamine 123 with ABCB1 (Sup Fig. 5). The results revealed a binding affinity of –8.977 kcal/mol for doxorubicin and –7.568 kcal/mol for Rhodamine 123, consistent with the binding trends observed in the MOE analysis. Comparative analysis of the docking poses revealed that doxorubicin forms multiple stabilizing interactions within the ABCB1 binding pocket, including hydrogen bonds with Glu875 and Gln347, as well as hydrophobic interactions with residues Met986 and Phe343, which support a tightly anchored conformation.

Additionally, we assessed the dynamic stability of the doxorubicin-ABCB1 complex using a 10-nanosecond molecular dynamics (MD) simulation. The Root Mean Square Deviation (RMSD) values of the ligand relative to its initial position were calculated (Fig. 6E). As shown in Fig. 6F, these values increased gradually during the first 5 ns, reaching a plateau with an RMSD value of 1.5 \AA , and remained stable for the remainder of the trajectory. The absence of large fluctuations or divergence implies that Dox retained a stable pose within the transmembrane domain within the binding site of ABCB1. A structural snapshot of the complex is shown in Fig. 6E, where the initial (green) and final (purple) poses of Dox are shown (overlaid). This illustrates that Dox remained stably embedded within the ABCB1 structure. Additionally, the ligand-binding cavity of ABCB1, formed by multiple α -helices, maintained its shape and continued to enclose the ligand. The overall structural integrity of the complex during the simulation supports the hypothesis that Dox is not only efficiently docked but also retained in a stable conformation, compatible with subsequent translocation, although further simulations would be required to capture the full transport cycle.

To complete the characterization of ABCB1, we analyzed breast cancer prognosis datasets from TCGA and GTEx using the GEPIA database⁴¹. The data revealed an association between high ABCB1 expression and reduced overall survival in breast cancer patients (Fig. 6G), supporting its role in doxorubicin resistance. Additionally, GEPIA analysis demonstrated a significant correlation between elevated eIF4E expression and poor overall survival in breast cancer patients (Fig. 6H). These observations were further validated using the KM-Plot database⁴². High eIF4E expression was associated with decreased survival in patients treated with doxorubicin across all breast cancer subtypes (Sup. Figure 4 A), with the effect being more pronounced in TNBC patients (Sup. Figure 4B).

To further elucidate the role of ABCB1 in breast cancer chemoresistance, we used verapamil, a well-recognized inhibitor of ABCB1, in functional and *in silico* analyses (Fig. 7). Given the high ABCB1 expression observed in the MDA_R variant, chemoresistant cells were treated with 1.6 μ M Dox for 12 h to induce ABCB1 overexpression, followed by co-treatment with verapamil at 10 μ M, an inhibitory concentration⁴³. Quantification of extracellular Dox levels revealed a significant reduction upon cotreatment (Fig. 7A), suggesting that verapamil effectively inhibited ABCB1-mediated Dox efflux. Moreover, the combined treatment with (Dox-verapamil) resulted in enhanced cytotoxicity under the same conditions (Fig. 7B), supporting the hypothesis that verapamil sensitizes resistant cells by impairing ABCB1 function.



To better understand the molecular basis of this inhibition, we performed molecular docking studies using the ABCB1 structure (PDB: 7A69) with Dox and verapamil (Fig. 7C, D). Both ligands were localized within the transmembrane domains (TMD1/2) of ABCB1, interacting with key residues, such as Gln347, Glu875, and Gln946, and positioning the anthracycline ring within the central substrate-binding cavity of ABCB1. A visual representation of the binding poses shows that doxorubicin (yellow) and verapamil (magenta) occupy nearly identical spatial positions within the ABCB1 binding site (blue), consistent with the overlapping interaction profile described above.

These findings reinforce the relevance of eIF4E as a contributor to chemoresistance and to tumor progression traits such as increased cell invasion. Notably, eIF4E may also play a regulatory role in the expression of the transcription factor Nrf2, a key target in antioxidant responses and chemoresistance. This potential interaction

Fig. 6. Doxorubicin chemoresistance is associated with the ABCB1 transporter. (A) Expression levels of ABCC1 in MDA_N and MDA_R cells under treatment with doxorubicin concentration range (0–1.6.6 μ M) through qPCR determination; (B) under the same conditions, characterization of ABCB1 levels. In both cases, GAPDH was used as a reference gene. Results showed three biological replicates' mean and standard deviation ($n=3$, $X \pm S.D.$). Molecular docking assay of ABCB1 (PDB: 7A69) under dox interaction, an increment in the interaction region is shown (C), and prediction of ABCB1 residues determinants of doxorubicin interaction obtained by MOE program (D). (E) Overlay of the ligand (doxorubicin) in its initial (green) and final (purple) conformations within the transmembrane binding pocket after a 10 ns molecular dynamics simulation. (F) RMSD of the ligand over the simulation time (10 ns), calculated with respect to the initial docking pose. (G) Overall survival plot for low and high expression of the ABCB1 gene in BC patients from GEPPIA. (H) The overall survival plot for low and high expression of eIF4E in breast cancer patients was obtained from the GEPPIA database (<http://gepia2.cancer-pku.cn/#index>). Data were statistically analyzed using one-way ANOVA and Newman–Keul's multiple comparison test **represents a p value <0.01 and *** p -value <0.001 .

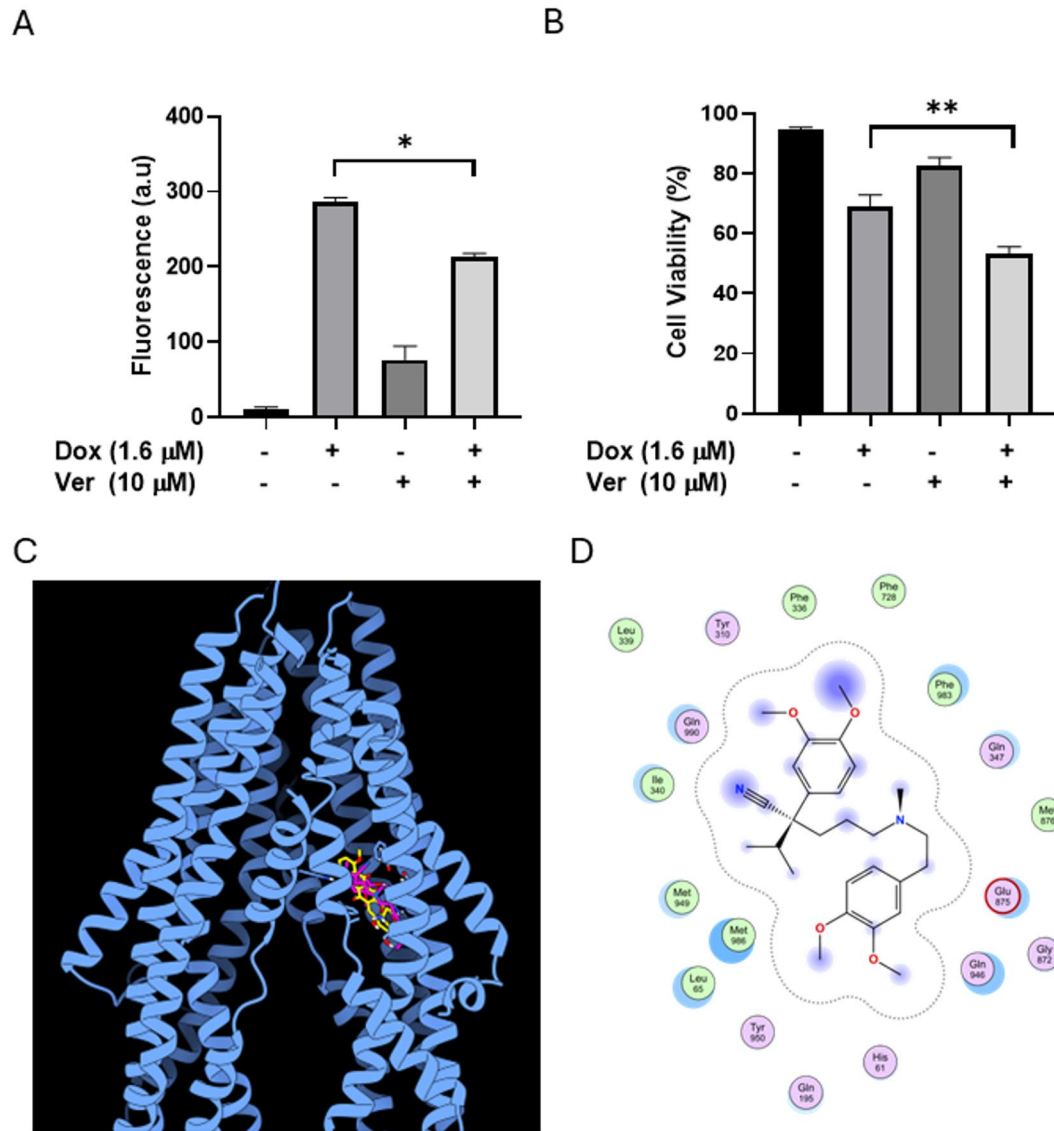


Fig. 7. Inhibition of ABCB1 with verapamil promotes significant cytotoxicity in MDA_R cells. (A) Evaluation of Dox efflux under 24 h treatment with dox (1.6 μ M) and concomitant treatment with the ABCB1 inhibitor (Verapamil) (10 μ M). (B) MTT viability assay under the same conditions. Molecular docking assay of ABCB1 (PDB: 7A69) under dox and verapamil interaction (C), an approach to the interaction region of the ligands dox (yellow) and verapamil (magenta) is shown (D), and prediction of ABCB1 residues determinants of verapamil interaction obtained by the MOE program. Results showed three biological replicates' mean and standard deviation ($n=3$, $X \pm S.D.$). Data were statistically analyzed using one-way ANOVA and Newman–Keul's multiple comparison test, * represents a p value <0.05 ** represents a p value <0.01 .

could influence the expression of ABC transporters, further impacting therapeutic response (personal communication).

Nrf2, a key factor in regulating chemoresistance

We evaluated Nrf2 expression to determine its potential association with ABCB1 regulation in MDA_N and MDA_R cells under the same range of doxorubicin concentrations (0–1.6 μ M) (Fig. 8A, B). The results suggest a correlation between Nrf2 and ABCB1 responses, particularly in MDA_R cells, wherein Nrf2 expression increased at the highest Dox dose (1.6 μ M). This phenomenon coincided with sustained eIF4E activity under the same treatment conditions. Complementary findings from a spheroid formation assay, used to assess proliferation capacity, supported this observation. At high Dox concentrations (1.6 μ M), spheroid formation was completely suppressed in MDA_N cells, whereas only a slight reduction in spheroid size was observed in MDA_R cells (Sup. Figure 5), suggesting preserved proliferative potential in the chemoresistant variant. This evidence suggests differential regulation of Nrf2 and ABCB1 mRNAs by the eIF4E/eIF4F complex in MDA_R cells, based on previous cytometry data and extracellular doxorubicin quantification assays.

To further investigate this regulatory axis, we employed siRNA-mediated knockdown of eIF4E to assess its downstream effects. Optimal knockdown conditions were established after 7 h of siRNA treatment, resulting in a reduction of eIF4E expression to 28% relative to control levels (Fig. 8C, D). Notably, this downregulation was accompanied by a significant decrease in MMP-9 activity in the extracellular medium (Fig. 8E, F), indicating a functional impact on invasive capacity.

We next evaluated the protein levels of eIF4E, eIF4E-p^{Ser-209}, and Nrf2 combined treatment with eIF4E siRNA and doxorubicin (1.6 μ M) for 12 h in both cell variants (Fig. 8G). Both MDA_N and MDA_R cells responded to siRNA treatment with a marked reduction in total eIF4E protein (Fig. 8G, H) and its phosphorylated form eIF4E-p^{Ser-209} (Fig. 8G, I), with the effect being particularly pronounced in MDA_R cells.

Importantly, under these same conditions, Nrf2 expression was also reduced in response to eIF4E knockdown, even in the presence of Dox (Fig. 8G). These results support the existence of a functional eIF4E/Nrf2 regulatory axis in doxorubicin-treated TNBC cells.

Interestingly, we have previously reported the involvement of Nrf2 in tamoxifen resistance in ER⁺ breast cancer cells⁴⁴, further reinforcing its role in treatment response across BC subtypes.

Effect of eIF4E regulation mediated by the molecule 4E1RCat

As a complementary approach to studying eIF4E regulation, we evaluated the effect of the eIF4E inhibitor 4E1RCat on TNBC cellular variants. We evaluated a range of doses of 4E1RCat (0.5–4 μ M) on key cell processes, including cell migration using the wound closure assay, as well as MMP-9 secretion in MDA_R cells. The results

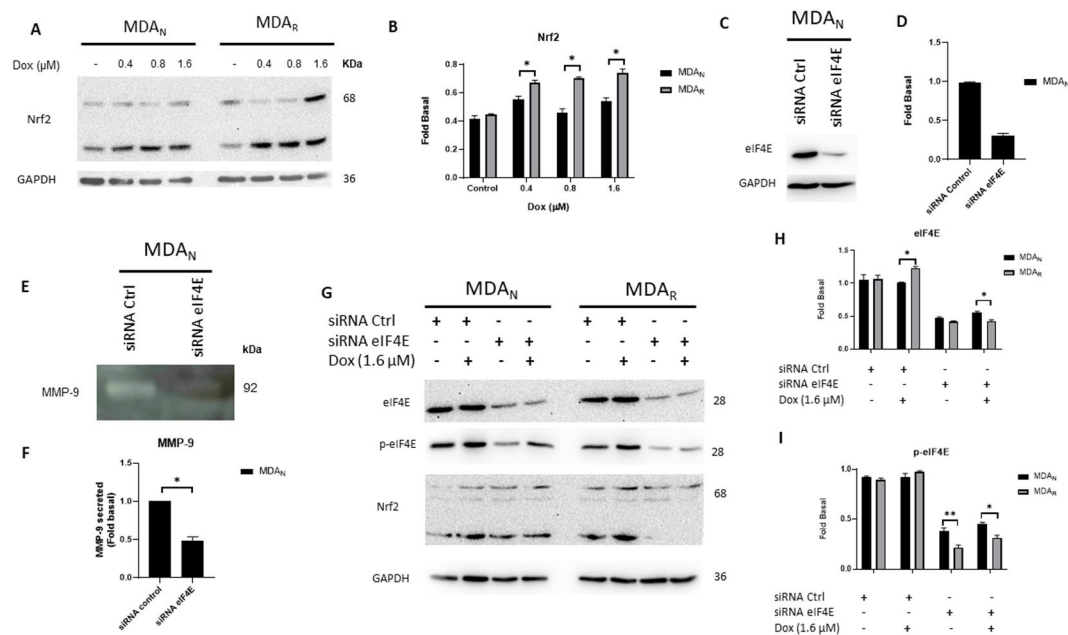


Fig. 8. Nrf2 is associated with the eIF4E expression. (A) WB evaluated Nrf2 protein expression levels in MDA_N and MDA_R variants under increasing dox concentrations (0–1.6.6 μ M); (B) Densitometry analysis of Nrf2. (C) WB of control eIF4E expression using siRNA on MDA_N cells with respective densitometric analysis (D). (E) MMP-9 activity was evaluated by zymography after treatment with siRNA eIF4E and densitometric analysis (F). (G) WB evaluated eIF4E, p-eIF4E, and Nrf2 expression under eIF4E siRNA and concomitant treatment with dox (1.6 μ M). Densitometric analysis of eIF4E (H) and p-eIF4E (I). Results showed three biological replicates mean and standard deviation ($n = 3$, $X \pm S.D.$). Data were statistically analyzed using one-way ANOVA and Newman–Keuls's multiple comparison test, *represents a p -value < 0.05 , and **represents a p value < 0.01 concerning the control. GAPDH was used as a loading control for WB.

led to the selection of 3 μ M as the optimal dose for eIF4E inhibition (Sup. Figure 7). Therefore, to further explore the relationship between ABCB1 expression and eIF4E activity, we analyzed the effect of 4E1RCat in the context of Dox treatment (1.6 μ M). As expected, Dox alone induced ABCB1 expression in both MDA_N and MDA_R cells, with a more pronounced effect in MDA_R (Fig. 9A). Interestingly, co-treatment with 4E1RCat (3 μ M) led to a decrease in ABCB1 expression only in MDA_N cells. In contrast, expression remained elevated in MDA_R cells despite treatment with the inhibitor (Fig. 9A).

These observations suggest that ABCB1 regulation in MDA_R cells may be less sensitive to eIF4E inhibition, possibly due to sustained phosphorylation of eIF4E at Ser209. Supporting this hypothesis, we detected higher eIF4E-p^{Ser-209} levels in MDA_R cells compared to MDA_N cells under both Dox (1.6 μ M) and Dox + 4E1RCat (3 μ M) treatments (Fig. 9B, C). This phenomenon indicates that the phosphorylation stage of eIF4E may play a pivotal role in maintaining ABCB1 expression in chemoresistant TNBC cells.

In silico docking simulations revealed that the binding site of 4E1RCat on the eIF4E structure (PDB: 4UED) shifts depending on the presence of the 4EBP1 peptide bound to the N-terminal region of eIF4E (Fig. 9D, E). The interaction between 4EBP1 and eIF4E is likely promoted under conditions of low 4EBP1 phosphorylation, as observed in MDA_N cells treated with increasing concentrations of doxorubicin (1.6 μ M) (Fig. 4A, D).

When 4EBP1 was included in the docking simulation, 4E1RCat was found to bind near Ser209, a residue associated with eIF4E activation through phosphorylation (Fig. 9D). In contrast, when 4EBP1 was excluded, representing a condition akin to MDA_R cells, where 4EBP1/2/3 phosphorylation prevents its binding to eIF4E; 4E1RCat was located near the cap-binding pocket, interacting with key residues such as Trp102 and Trp56 on the eIF4E structure (Fig. 9E).

These structural insights support the hypothesis that phosphorylation-dependent accessibility of eIF4E domains modulates the binding mode of 4E1RCat, potentially influencing its inhibitory efficacy in different TNBC cellular contexts.

Discussion

TNBC is characterized by poor prognosis and frequent development of chemoresistance. To model this clinically relevant feature, we established a new strategy to generate a doxorubicin-resistant variant of the MDA-MB-231 TNBC cell line. By treating the parental line (referred to as MDA_N) with the IC₂₅ dose of doxorubicin, we were able to develop a chemoresistant variant, MDA_R (Fig. 1). The MDA_R cells exhibited a 3.1-fold increase in IC₅₀ compared to MDA_N cells, suggesting their resistant phenotype. Significantly, the IC₅₀ of doxorubicin in MDA_N cells (0.619 μ M) falls within the range reported in breast cancer patients (0.023–1.14 μ M)⁴⁵. In contrast, the MDA_R IC₅₀ (1.8 μ M) exceeds this clinical range, further supporting its resistance status. This approach appears to provide an innovative platform for modeling acquired chemoresistance, particularly for compounds or regimens

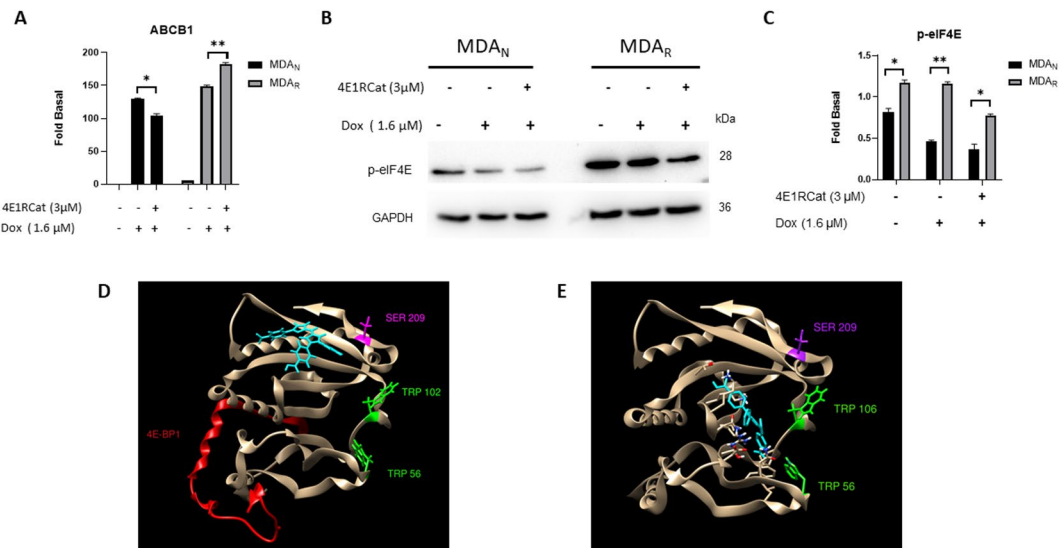


Fig. 9. The eIF4E/ABCB1 axis in chemoresistance, the role of the 4E1RCat molecule. (A) Expression levels of ABCB1 in MDA_N and MDA_R cells under treatment with dox (1.6 μ M) and 4E1RCat (3 μ M) for 48 h through qPCR determination, GAPDH was used as a reference gene. (B) p-eIF4E expresión levels evaluated by WB under dox (1.6 μ M) and 4E1RCat (3 μ M) concomitant treatment, MDA_N and MDA_R variants were treated for 48 h. (C) Densitometry analysis of p-eIF4E; Results showed three biological replicates' mean and standard deviation ($n=3$, $X \pm S.D.$) and expressed as % of control; data were statistically analyzed using one-way ANOVA and Newman–Keuls's multiple comparison test ** represents a p -value < 0.01 concerning the control. GAPDH was used as a control. (D, E) Molecular docking assay of eIF4E (PDB used 4UED) under 4E1RCat and concomitant interaction of 4E1RCat and 4EBP-1. Cyan: eIF4E, Green: Tryptophan, Red: 4E Binding Protein –1.

with high cytotoxicity, wherein resistance development is often limited under standard culture conditions⁴⁶. Our model could serve as a foundation for testing therapeutic strategies targeting resistance mechanisms in TNBC.

Evidence suggested improved doxorubicin handling in the MDA_R variant compared to the parental MDA_N cells (Fig. 2). Despite its well-documented side effects, doxorubicin remains a first-line anthracycline used in breast cancer treatment. However, while initially effective, the development of chemoresistance can reduce its efficacy and is often associated with increased tumor aggressiveness⁴⁷. To explore this phenomenon, we performed a series of cell biology assays aimed at characterizing key features of resistance. Notably, TNBC is known for its high metastatic potential, a trait that is further exacerbated in cases of chemoresistance⁴⁸.

The development of chemoresistance following prolonged exposure to chemotherapeutic agents is commonly associated with an enhanced ability of tumor cells to migrate and metastasize^{44,49}. The data obtained in this study are consistent with these observations, as demonstrated by our *in vitro* experiments (Fig. 3). However, additional validation using *in vivo* models would be necessary to gain a more comprehensive understanding of the mechanisms involved.

The results indicate enhanced migratory activity in MDA_R cells compared to the parental MDA_N variant. Notably, low concentrations of doxorubicin (0.05–0.8 μ M) promoted migration in MDA_R cells. This finding is in agreement with previous reports showing that sub-cytotoxic doses of Dox can activate the Src signaling pathway, thereby promoting cell motility⁵⁰. The concentrations used in this study are within the range reported in plasma samples from breast cancer patients⁴³, suggesting clinical relevance. Importantly, invasive behavior and MMP-9 secretion were maintained in MDA_R cells even under high Dox concentrations (0.8–1.6 μ M) (Fig. 5), in contrast to the marked suppression observed in MDA_N cells. This pattern was further supported by spheroid formation assays, in which MDA_R cells retained the ability to form spheroids despite Dox exposure, whereas MDA_N cells showed complete suppression (Sup. Figure 5).

Additionally, we evaluated doxorubicin internalization and elimination. MDA_N cells showed a reduced capacity for drug efflux, as evidenced by lower levels of extracellular Dox. In contrast, MDA_R cells retained greater viability and higher extracellular Dox levels following treatment, particularly at elevated concentrations (Fig. 2). These findings may indicate that MDA_R cells have acquired adaptive mechanisms that counteract the cytotoxic effects of high Dox concentrations. One key contributor to this phenotype could be the ABCB1 transporter, which may mediate enhanced drug efflux and confer chemoresistance.

The implication of the ABC transporters as a determinant of chemoresistance, in this instance ABCB1 expression, was significantly induced by Dox in a dose-dependent manner, with MDA_R cells exhibiting significantly greater upregulation in comparison with MDA_N cells. This supports the notion that ABCB1 acts as a major mediator of Dox efflux and resistance. Molecular docking simulations confirmed a specific interaction between Dox and key residues in ABCB1's transmembrane domains, including Leu236, Glu243, and Lys826. These interactions were stabilized by hydrogen bonding and van der Waals forces, suggesting a high-affinity binding conformation. Further validation with Rhodamine 123, a known ABCB1 substrate, showed a partial overlapping, reinforcing the selectivity of Dox for this transporter. AutoDock Vina simulations revealed a stronger binding affinity for Dox (-8.977 kcal/mol) compared to Rhodamine 123 (-7.568 kcal/mol), which is consistent with its tighter docking profile. Importantly, molecular dynamics simulations over a 10- nanosecond trajectory supported these findings, revealing minimal ligand displacement and sustained retention of Dox within the transmembrane cavity.

Moreover, despite the importance of verapamil, the exact site where it binds to the ABCB1 structure has not been described. Importantly, we observed that the inhibition of ABCB1 with verapamil at the MDA_R reduces the export of Dox. This process was coupled with cell viability (Fig. 7). A Molecular Docking assay supported this interpretation, revealing that Doxorubicin and verapamil bound to the same region of the ABCB1 binding pocket, which is consistent with the hypothesis that verapamil inhibits Doxorubicin efflux by competitively occupying the same site. Although we do not rule out the possibility that other transporters and Dox resistance mechanisms may be involved, the data underscore the likely importance of ABCB1, and therefore of the mechanisms that regulate its expression.

Results suggest that ABCB1 mediated drug efflux represents one axis of chemoresistance, which might be further reinforced by translational control mechanisms, such as eIF4E regulation and changes in 4EBP activity in the presence of doxorubicin. Therefore, we investigated how eIF4E is modulated in response to doxorubicin. Our data indicates that both eIF4E expression and its phosphorylated form (eIF4E-p^{Ser-209}) were maintained as Dox concentration increased, particularly in the MDA_R variant. This may suggest that eIF4E activity is preserved in chemoresistant cells under therapeutic stress. While our primary focus was on eIF4E, we acknowledge that further exploration of the MAPK signaling pathway, including p38/MNK activation⁵⁰, could provide additional insight into the mechanisms sustaining eIF4E phosphorylation. In parallel, eIF4E regulation appears to be linked to a reduction in the phosphorylation of its modulatory binding proteins, 4EBP1/2/3, as evidenced by our data (Fig. 4A, D). These findings point toward an adaptive response in the eIF4F complex in MDA_R cells, reflecting dynamic regulation in response to Dox treatment.

Moreover, our analysis of protein–protein interactions using the STRING database (<https://string-db.org/>)⁵¹ supports the potential functional relevance of the MNK–eIF4E signaling axis in the context of chemoresistance. The interaction network highlights high-confidence associations among eIF4E, its upstream kinases MNK1 and MNK2, and the scaffolding protein eIF4G1, which facilitates eIF4E phosphorylation at Ser209. This post-translational modification has been implicated in the selective translation of mRNAs involved in cell survival and stress response pathways (Sup. Figure 6). Among the candidate downstream targets, Nrf2 emerges as a plausible effector, as previous studies have suggested its translation may be regulated by eIF4E activity¹⁶. In turn, Nrf2 is known to transcriptionally activate ABCB1, a key transporter associated with drug efflux and chemotherapy resistance^{52,53}. This interaction patterns align with the model proposed in this study, in which sustained eIF4E

activity could contribute to increased ABCB1 expression via a Nrf2-dependent mechanism, ultimately reducing intracellular doxorubicin levels and contributing to the chemoresistant phenotype observed in MDA_R cells.

Our data suggests that the translation factor eIF4E remains functionally active at elevated doxorubicin concentrations in MDA_R cells, promoting the selective translation of targets such as Nrf2 and ABCB1. The sustained activity of the mTOR/eIF4E axis at 1.6 μ M, above clinically reported plasma concentrations, appears to correlate with increased cellular invasion (Fig. 5). Additionally, lipid overload has been proposed to potentiate these oncogenic processes^{13,54}. In previous work, we demonstrated the role of eIF4E as a key regulator of protein synthesis and lipogenesis, establishing a link between eIF4E activity, mRNA processing, and carcinogenesis, with potential implications for chemoresistance. This hypothesis is further supported by the results of our eIF4E siRNA experiments, which showed that silencing eIF4E impairs downstream targets and reduces cellular invasion and survival pathways (Fig. 8), reinforcing its possible role as a central mediator of the chemoresistant phenotype.

As a complementary approach, we employed a small molecule-based regulatory strategy targeting eIF4E. Treatment with the eIF4E inhibitor 4E1RCat⁵⁵ further supports the potential involvement of eIF4E in chemoresistance mechanisms, as evidenced by changes in ABCB1 expression (Fig. 9). Additionally, our docking simulations provided further insight into the structural interactions between eIF4E, 4EBP1, and 4E1RCat. The results suggest that the presence of 4EBP1 promotes the localization of 4E1RCat near Ser209, a key regulatory site on eIF4E, thereby potentially inhibiting its activity. This observation is consistent with the experimental data presented in Fig. 9. Nonetheless, further validation using three-dimensional structural analyses, such as crystallography, would help to strengthen our understanding of the binding interactions and inhibitory mechanism of 4E1RCat on eIF4E.

4E1RCat inhibits the translation process by competing with the eIF4G binding site on eIF4E, thereby preventing the formation of the eIF4F complex. This mechanism allows for the direct evaluation of eIF4E functional involvement and its regulatory relationship with downstream proteins that rely on its activity⁵⁵. Other molecules, such as Ribavirin, have shown similar effects on eIF4E function, although through indirect mechanisms⁵⁶. Our findings support the activation hypothesis of the eIF4E–Nrf2–ABCB1 axis in MDA_R cells, which may contribute to the observed chemoresistance phenotype. Previous data from our group have also indicated a Nrf2-dependent transition from an ER⁺ phenotype to a TNBC-like profile in response to tamoxifen-derived metabolites⁴⁴. Building on this evidence, our team is currently developing Nrf2 inhibitors through in silico screening and molecular docking approaches using a large chemical compound library. These efforts aim to identify compounds capable of targeting Nrf2 as a strategy to overcome doxorubicin resistance in TNBC MDA_R cells (personal communication).

An additional therapeutic strategy might involve the concomitant inhibition of eIF4E and MNK kinases, which could effectively disrupt eIF4E function and allow for a more precise assessment of its impact on ABCB1 expression. Alternatively, the use of Proteolysis Targeting Chimeras (PROTACs) represents a promising approach to selectively degrade eIF4E, thereby enabling functional studies on the eIF4E–Nrf2–ABCB1 axis. Such strategies could provide valuable insights into the translational regulation underlying doxorubicin resistance in TNBC, supporting the development of targeted therapeutic interventions.

Our research team plans to further evaluate the eIF4E–Nrf2–ABCB1 axis in *in vivo* models to validate the functional relevance of our findings. We will use the BALB/c murine model, in which 4T1 cells will be orthotopically inoculated. To assess the specific role of eIF4E, we will employ CRISPR–Cas9 genome editing to generate eIF4E knockout in 4T1 cells, enabling the evaluation of its impact on chemoresistance and metastatic potential. These experiments are expected to provide essential validation of our *in vitro* observations.

Specifically, our results suggest that sustained eIF4E expression in MDA_R cells is associated with the enhanced translation of the drug efflux transporter ABCB1, contributing to reduced intracellular doxorubicin accumulation. Therefore, our findings point toward the involvement of the eIF4E–Nrf2–ABCB1 axis in chemoresistance and identify potential molecular targets for both pharmacological and genetic modulation. To provide an integrative perspective, Fig. 10 summarizes the main mechanisms proposed in this work, highlighting the interplay between eIF4E activation, Nrf2 regulation, and ABCB1-mediated efflux. This schematic representation offers a visual overview of our proposed model of chemoresistance, facilitating the interpretation of how translational control and stress response pathways converge in TNBC.

Methods

Cell culture

The triple-negative breast cancer cell line MDA-MB-231 from the American Type Culture Collection (ATCC HTB-26) was used as the parental cell line to generate the doxorubicin-resistant cell variant and the internal control to perform comparative studies. Unless otherwise stated, cells were proliferated in a DMEM medium supplemented with fetal bovine serum (FBS) and 10% antibiotics (50 U/mL penicillin and 50 μ g/mL streptomycin).

Generation of the doxorubicin-resistant cell variant

In this work, we decided to evaluate the MDA-MB-231 cell line since it is classified as a mesenchymal stem-like cell, which allows us to study the molecular phenomena associated with chemoresistance⁵⁷. Then, we implemented three protocols to generate the doxorubicin-resistant cell variant. The first consisted of treatment with increased concentrations of doxorubicin, with an initial dose of 0.05 μ M. Treatment periods of 4–6 days were performed, and a recovery period of 20–30 days was made. In this case, the protocol was based on the experimental approach established by García-González et al.⁵⁴ with modifications.

In the second one, the IC₅₀ of the parental cell line was confirmed (0.6 μ M) by performing a dose-response assay using increasing concentrations of doxorubicin (0–3.2.2 μ M). Later, cells were treated with half-maximal

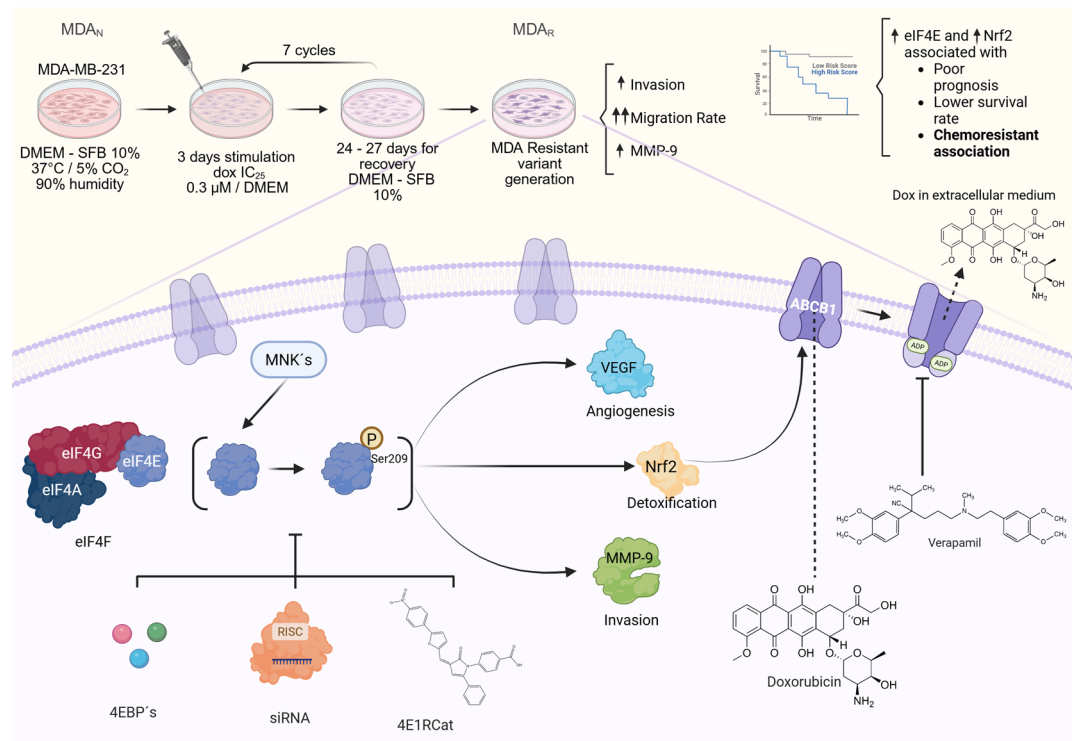


Fig. 10. Integrative model of the eIF4E–Nrf2–ABCB1 axis in doxorubicin resistance. Schematic summary of the proposed mechanism by which sustained eIF4E activation in MDA_R cells promotes the selective translation of Nrf2 and ABCB1, enhancing antioxidant response and drug efflux. The convergence of translational control and stress-adaptive signaling reduces intracellular doxorubicin accumulation, thereby reinforcing the chemoresistant phenotype in triple-negative breast cancer cells.

inhibitory concentration IC_{50} (0.6 μ M of doxorubicin) for 3 days and a recovery period of 3–4 weeks; this protocol was performed seven times. However, for this protocol, only the IC_{50} value was suitable. Finally, in the third protocol (Fig. 1A), the doxorubicin-resistant cells obtained were reached using treatments with the doxorubicin IC_{25} (0.3 μ M) for 72 h and a recovery period of 24–27 days. This treatment scheme was implemented for 7 cycles. Cells were maintained under a low dox concentration (15 nM) during the recovery and proliferation periods. This variant generated under the scheme of IC_{25} was named MDA_R, and as a control, we evaluated the parental MDA-MB-231 cells denominated as MDA_N cells.

Cell viability assays

3-(4,5-dimethylthiazol-2-yl)-2,5-diphenyltetrazolium bromide (MTT) reduction assays were used with a modification to the protocol of Hernandez-Valencia et al.⁴⁶ to evaluate the chemoresistance. Proliferating cells were seeded in 24-well plates at a density of 40,000 cells per well with 500 μ L of supplemented DMEM medium for 24 h at 37 °C/5% CO₂. Cell cultures were maintained in a non-supplemented DMEM medium for 24 h. Then, cell cultures were treated with increasing doxorubicin concentrations (0.05–6.4 μ M) for 48 h. In addition, the effect of concomitant treatment of Dox (1.6 μ M) and verapamil (10 μ M) for 24 h was characterized. Later, 250 μ L per well of MTT solution (0.5 mg/mL of MTT dissolved in non-supplemented DMEM medium) was added, and the plate was incubated at 37 °C/5% CO₂ for 3 h. The medium was removed, and the cell monolayer was lysed with 250 μ L of DMSO, collected in 1.5 mL conical tubes, and centrifuged at 2504 $\times g$ for 10 min at 20 °C. Absorbance measures were collected at 595 nm.

Doxorubicin internalization by cytometer analysis

Cells were incubated under several treatments with doxorubicin in a DMEM medium for 24 h, with a previous fasting period of 24 h. Next, the cells were washed twice with PBS 1X. The monolayer recovered in PBS (300 μ L), and the cell suspension was mixed gently. Cellular characterization was performed in a Beckman-Coulter cytometer Cytoflex (Pasadena, CA, USA); 15,000 events were characterized using the PC7-A filter to record doxorubicin-associated fluorescence, and median fluorescence intensity was used for analysis^{37,58,59}.

Dox quantification in extracellular media

Cell cultures were grown to reach a confluence of 90% in the complete DMEM medium. Cultures were fasted for 24 h with a non-supplemented medium. Stimuli with increasing dox concentrations (0–1.6.6 μ M) were prepared in OptiMEM medium, low in phenol-Red. Cells were incubated for 24 and 48 h. Likewise, we performed experiments under the treatment with verapamil molecule (10 μ M), a reported ABCB1 inhibitor; we evaluated

its effect on Dox cellular exportation. Supernatants were collected and centrifuged at 3170 xg at 4 °C for 10 min, for cellular detritus elimination. Supernatants were collected and centrifuged at 3170 xg at 4 °C for 5 min. The supernatant was collected and evaluated in a CaryEclipse Variant fluorometer (Agilent Technologies, Inc., Santa Clara, CA, USA) with a 470 nm and 595 nm excitation and emission wavelength, respectively. A standard curve was constructed to ascertain the concentration.

Wound-healing migration assays

The effect of doxorubicin chemoresistance on migration was evaluated by wound healing assay as described by Leal-Orta et al.⁶⁰. Cells were seeded in 6-well dishes at a density of 200,000 cells per well and incubated at 37 °C/5% CO₂ for 48 h until complete confluence was reached. The medium was removed, and 1 mL of non-supplemented DMEM medium was plated for 24 h. Before stimulation, cells were pretreated with mitomycin-C for 2 h (8 µg/mL). Wound healing was performed using a sterile 200 µL tip, two washes with PBS were performed, and cells were incubated for 48 h with several treatments. Positive control DMEM medium supplemented with 10% FBS and negative control with non-supplemented DMEM were included. After 48 h, supernatant media was collected for zymogram assays, and the cells were fixed with cold methanol for 10 min under gentle agitation at 4 °C. Methanol was removed, and the cells were stained with Coomassie blue for 10 min under gentle agitation at 4 °C. Final washes were performed with cold PBS and observed under an inverted microscope.

Invasion assays

The modified transwell method performed invasion experiments in 24-well plates containing 12 cell culture inserts with 8 µm pore size (NEST, Wuxi Nest Biotechnology Co. Jiangsu, China). Briefly, 50 µL of BD Matrigel (Corning, Somerville, MA, USA) was added into culture inserts and maintained at 37 °C for 45 min. MDA_N and MDA_R cells were plated at 1 × 10⁵ cells per insert in serum-free DMEM on the top chamber. The lower chamber contained 600 µL DMEM and FBS 10% with the doxorubicin range treatment concentration (0–1.6.6 µM). DMEM medium with FBS 10% was used as a positive control; Boyden chambers were incubated for 48 h at 37 °C in a 5% CO₂ atmosphere. Then, cells and matrigel on the upper surface of the membranes were removed with cotton swabs, and the cells on the lower surface of the membrane were washed and fixed in methanol for 5 min⁶¹; three biological replicates were performed for statistical analysis.

qPCR

MDA_N and MDA_R cellular variants under 90% confluence were treated under the specific schemes. Then, total RNA from cellular variants was obtained with Trizol reagent, following the supplier's instructions. cDNA was synthesized using 1 µg of RNA and the Primer Script RT-PCR Kit (Takara Inc, Tokyo, Japan). cDNA concentration was standardized for qPCR with the PowerUp Sybr Green Master Mix 2X (Applied Biosystems, Waltham, MA, USA) according to the manufacturer's instructions, and 4 µL of the resultant cDNAs were used for each PCR reaction (62). Primers sequences were ABCB1 forward 5'-GCCAGCTGAACCTCTTAGAC-3, ABCB1 reverse 5'-GATTCGTGCACAGCAGCA-3, ABCC1 forward 5'-GGCTCAAGGAGTATTAGAG-3, ABCC1 reverse 5'-CCATCG ATGATGATCTCTCC-3, GAPDH forward 5'-AGACAGCCGCATCTCTGT3', and GAPDH reverse 5'-CTTGGCGTGGGTAGAGTCAT3'. qPCR reactions were performed in triplicate using an ABI PRISM 7000 sequence detection system (Applied Biosystem); data were analyzed using the 2-ΔΔC_t method with GAPDH as a reference calibrator and reported as fold change.

Immunoprecipitation (IP) assays

MDA_N and MDA_R cell cultures were treated under an increasing doxorubicin concentration range (0–1.6.6 µM). For these experiments, 250 µg of protein cell lysates were used. For the total protein lysates, 2 µL of anti-eIF4E (sc-9976) was employed. All samples were incubated for 3 h at 4 °C with mild agitation. Further, 10 µL of protein A/G plus agarose (sc-2003) was added, and incubation was maintained for 12 h at 4 °C with mild agitation. Then, samples were centrifuged at 1,409 xg for 5 min at 4 °C. The supernatant was discarded. The obtained pellets were resuspended and washed with mild agitation using STE 1x buffer (TBS, EDTA 100 mM, NP40 10%), and centrifugation at 1,409 xg for 5 min was made. This process was performed twice. Next, 40 µL of Laemmli buffer 1x was added to the pellet, mild mixing, and heated for 2 min at 90 °C. The solution was centrifuged at 1,409 xg for 3 min. Immune complexes were evaluated, as well as SDS-PAGE, PVDF transference, and western-blot identification by processing 20 µL of the supernatant samples. GAPDH was used as a loading protein.

Molecular docking

The atomic coordinates of the protein ABCB1, Protein Data Bank (PDB) ID: 7A69, with a resolution of 3.2 Å, were used for molecular docking experimentation. The structure of doxorubicin (CID 31703) and verapamil (2520) was obtained from the PubChem database. The protein structure was prepared; water and small molecules were removed. Ligands and proteins were 3D protonated, and energy was minimized using a Molecular Operating Environment (MOE) with default parameters (Placement: Triangle Matcher, Rescoring 1: London G, AMBER99 forcefield). Each ligand was generated by many different conformations, and the protein was visualized using the ligand interactions implemented in MOE. A similar strategy was used for ABCC1 characterization (PDB 6UY0) with doxorubicin. For the characterization of the eIF4E factor, the PDB structure 4UED was evaluated, including the interaction with 4E-BP1 and the small molecule 4E1RCat (CID 1619554). Docking results are analyzed using the S-score values.

The S-score in the Molecular Operating Environment (MOE) is a composite scoring function used to estimate the binding affinity between a ligand and a protein target during molecular docking simulations. It integrates multiple energetic terms, including van der Waals interactions, electrostatics, hydrogen bonding, desolvation, and torsional strain, to approximate the free energy of binding. The score is expressed in arbitrary

units correlating with binding strength, where more negative values suggest more favorable ligand-receptor interactions.

AutoDock Vina (version 1.2.7). The crystal structure of human ABCB1 is the same as MOE and was prepared by removing water molecules and non-essential co-crystallized ligands. Polar hydrogens were added, and Gasteiger charges were assigned using AutoDock Tools 1.5.7 (ADT). Ligands, including Doxorubicin and Rhodamine 123, were prepared in their energy-minimized conformations, and torsional flexibility was defined within ADT.

A grid box was defined to encompass the transmembrane substrate-binding region of ABCB1, with dimensions of $73 \times 92 \times 82$ Å. Docking was performed using default Vina parameters with an exhaustiveness level of 8, and the top-scoring binding pose (lowest binding free energy) was selected for further analysis. Binding affinities were recorded in kcal/mol, and ligand–protein interactions were visualized using MOE.

SiRNA experimentation

Cells were seeded at a density of 7.5×10^4 cells/plates and incubated overnight in a standard growth medium without antibiotics. eIF4E siRNA (h) (sc-35284) and control siRNA-A (sc-37007) were purchased from Santa Cruz Biotechnology (Santa Cruz, CA, USA). Transfection was performed according to the following conditions: 4 µL of siRNA was diluted on 50 µL of transfection medium (Solution A), on the other hand, the transfection reactive (3 µL) was homogenized with 50 µL of transfection (Solution B). Then, solution A was added to solution B, mixed kindly, and incubated for 30 min at room temperature. Next, 400 µL of transfection was added and mixed, and 500 µL of total solution was added per well. Cells were incubated at 37 °C for 6 h, and 500 µL of complete medium (2x) was added and incubated for 24 h. The medium was withdrawn, and 500 µL of complete medium (1x) for 12 h, subsequently dox treatment was added. After verifying the transfection efficiency by WB, experimentation with dox was performed using a final concentration of dox 1.6 µM and 12 h treatment.

Zymography

MDA_N and MDA_R cell cultures were incubated under different treatments, and the conditioned medium was collected. Volumes of 40 µL non-heated conditioned medium samples were mixed with 5× sample buffer (0.313 M Tris pH 6.8, 10% SDS, 50% glycerol, and 0.05% bromophenol blue) and processed on 8% polyacrylamide gels copolymerized with gelatin (1% w/v). Gels were rinsed twice with 2.5% Triton X-100 and then incubated in a development buffer (50 mM Tris–HCl pH 7.4, 10 mM CaCl₂, and 0.02% NaN₃) for 48 h at 37 °C. Gels were fixed and stained with 0.25% Coomassie Brilliant Blue G-250 in 10% acetic acid and 30% methanol. Proteolytic activity was detected as clear bands against the background stain of the unprocessed substrate.

GEPIA analysis

We used the GEPIA database to evaluate the potential implications of protein targets eIF4E and ABCB1 in breast cancer. We analyzed the mRNA expression levels of eIF4E (EIF4E coding gene, Gene ID: 1977) and ABCB1 (ABCB1 coding gene, Gene ID: 5243) and their relationship with overall survival in BC patients using GEPIA, which collects information from the The Cancer Genome Atlas (TCGA)and GTEx (Genotype-Tissue-Expression)^{41,63}.

KM-PLOT analysis

Similarly, we use the KM-plot database⁴² to evaluate the implication of eIF4E protein (UniProt ID: P06730) expression and its relationship with survival TNBC patients and TNBC patients with dox treatment. We selected the TCGA-RPPA database for the KM analysis.

Molecular dynamics (MD)

MD simulation was performed using the QwikMD 1.3 plugin⁶⁴ in VMD and the NAMD 2.14 simulation engine⁶⁵ to evaluate the stability of the ABCB1-Dox complex derived from molecular docking. The simulation was carried out in an explicit solvent to streamline the analysis and avoid the added complexity of embedding the transmembrane protein in a lipid bilayer. Harmonic positional restraints were applied to the Ca atoms of the protein throughout the simulation to preserve the overall architecture of the transmembrane pore in the absence of a bilayer membrane environment.

The ABCB1-Dox complex was solvated in a rectangular box of TIP3P water molecules with an 18 Å buffer, and the system was neutralized with Na⁺ and Cl⁻ ions to achieve a physiological ionic strength of 0.15 M. The CHARMM36 force field was used for the ABCB1 protein. The Dox topology and parameters were generated using CHARMM-GUI⁶⁶however, due to the structural complexity of this ligand, several parameters were missing or incorrect, including bond definitions, angles, dihedrals, and improper torsions, which all were manually corrected prior to simulation.

The ligand-receptor system was subjected to energy minimization (20,000 steps), followed by annealing in the NPT ensemble (0.24 ns, heating from 60 K to 298 K), and equilibration (1.0 ns) at 298 K and 1 atm using the Nosé–Hoover Langevin piston. A production MD run of 10 ns was then performed under NPT conditions at 298 K. The r-RESPA multiple time step scheme was used, with short-range interactions updated every single step and long-range electrostatics every two steps. A 2 fs integration time step was used, and long-range electrostatic interactions were computed using the particle mesh Ewald (PME) method. All bonds involving hydrogen atoms were constrained using the SHAKE algorithm. The analysis tools included in QwikMD were used to calculate RMSD.

Data availability

Data is contained within the article.

Received: 28 February 2025; Accepted: 2 December 2025

Published online: 07 January 2026

References

1. Łukasiewicz, S. et al. Breast cancer—epidemiology, risk factors, classification, prognostic markers, and current treatment strategies—An updated review. *Cancers* **13**, <https://doi.org/10.3390/cancers13174287> Preprint at (2021).
2. Siegel, R. L., Giaquinto, A. N. & Jemal, A. Cancer statistics, 2024. *CA Cancer J. Clin.* **74**, 12–49 (2024).
3. Kunc, M., Biernat, W. & Senkus-Konefka, E. Estrogen receptor-negative progesterone receptor-positive breast cancer – Nobody's land or just an artifact? *Cancer Treatment Reviews* vol. **67** 78–87 Preprint at (2018). <https://doi.org/10.1016/j.ctrv.2018.05.005>
4. Kumar, P. & Aggarwal, R. An overview of triple-negative breast cancer. *Archives of Gynecology and Obstetrics* vol. **293** 247–269 Preprint at (2016). <https://doi.org/10.1007/s00404-015-3859-y>
5. Yin, L., Duan, J. J., Bian, X. W. & Yu, S. C. Triple-negative breast cancer molecular subtyping and treatment progress. *Breast Cancer Research* **22** <https://doi.org/10.1186/s13058-020-01296-5> Preprint at (2020).
6. Hanahan, D. & Weinberg, R. A. Hallmarks of cancer: The next generation. *Cell* **144** 646–674 <https://doi.org/10.1016/j.cell.2011.02.013> Preprint at (2011).
7. Kannampuzha, S. & Gopalakrishnan, A. V. Cancer chemoresistance and its mechanisms: associated molecular factors and its regulatory role. *Med. Oncol.* **40**, 264 (2023).
8. Palomeras, S., Ruiz-Martínez, S. & Puig, T. Targeting breast cancer stem cells to overcome treatment resistance. *Molecules* vol. **23** Preprint at. <https://doi.org/10.3390/molecules23092193> (2018).
9. Fisusi, F. A. & Akala, E. O. Drug combinations in breast cancer therapy. *Pharm. Nanotechnol.* **7**, 3–23 (2019).
10. Bai, X., Ni, J., Beretov, J., Graham, P. & Li, Y. Triple-negative breast cancer therapeutic resistance: Where is the Achilles' heel? *Cancer Letters* vol. **497** 100–111 Preprint at. <https://doi.org/10.1016/j.canlet.2020.10.016> (2021).
11. Nedeljković M, Damjanović A. Mechanisms of Chemotherapy Resistance in Triple-Negative Breast Cancer-How We Can Rise to the Challenge. *Cells*. 2019 Aug 22;8(9):957. doi: 10.3390/cells8090957
12. An, J., Peng, C., Tang, H., Liu, X. & Peng, F. New advances in the research of resistance to neoadjuvant chemotherapy in breast cancer. *International Journal of Molecular Sciences* vol. **22** Preprint at. <https://doi.org/10.3390/ijms22179644> (2021).
13. Gonzalez-Ortiz, A., Galindo-Hernandez, O., Hernandez-Acevedo, G. N., Hurtado-Ureta, G. & Garcia-Gonzalez, V. Impact of cholesterol-pathways on breast cancer development, a metabolic landscape. *Journal of Cancer* vol. **12** 4307–4321 Preprint at. <https://doi.org/10.7150/jca.54637> (2021).
14. Malka-Mahieu, H., Newman, M., Désaubry, L., Robert, C. & Vagner, S. Molecular pathways: The eIF4F translation initiation complex-newopportunities for cancer treatment. *Clinical Cancer Research* vol. **23** 21–25 Preprint at. <https://doi.org/10.1158/1078-0432.CCR-14-2362> (2017).
15. Hanahan, D. Hallmarks of Cancer: New Dimensions. *Cancer Discovery* vol. **12** 31–46 Preprint at. <https://doi.org/10.1158/2159-8290.CD-21-1059> (2022).
16. Muñoz-Ayala, A. & Chimal-Vega, B. García-González, V. Translation initiation and its relationship with metabolic mechanisms in cancer development, progression and chemoresistance. *Adv. Protein Chem. Struct. Biol.* **132**, 111–141 (2022).
17. Romagnoli, A. et al. Control of the eIF4E activity: structural insights and pharmacological implications. *Cellular and Molecular Life Sciences* vol. **78** 6869–6885 Preprint at. <https://doi.org/10.1007/s0018-021-03938-z> (2021).
18. Peter, D. et al. Molecular architecture of 4E-BP translational inhibitors bound to eIF4E. *Mol. Cell.* **57**, 1074–1087 (2015).
19. Maracci, C. et al. The mTOR/4E-BP1/eIF4E signalling pathway as a source of cancer drug targets. *Curr. Med. Chem.* **29**, 3501–3529 (2022).
20. Yang, X., Zhong, W. & Cao, R. Phosphorylation of the mRNA cap-binding protein eIF4E and cancer. *Cell. Signal.* **73**, Preprintat^{https://doi.org/10.1016/j.cellsig.2020.109689} (2020).
21. Zheng, J., Li, X., Zhang, C. & Zhang, Y. eIF4E Overexpression Is Associated with Poor Prognoses of Ovarian Cancer. *Analytical Cellular Pathology* **2020**. (2020).
22. Tang, Y. et al. Overexpression of p-4EBP1 associates with p-eIF4E and predicts poor prognosis for non-small cell lung cancer patients with resection. *PLoS One* **17(6): e0265465**. <https://doi.org/10.1371/journal.pone.0265465> (2022).
23. Shveygert, M., Kaiser, C., Bradrick, S. S. & Gromeier, M. Regulation of eukaryotic initiation factor 4E (eIF4E) phosphorylation by Mitogen-Activated protein kinase occurs through modulation of MnK1-eIF4G interaction. *Mol. Cell. Biol.* **30**, 5160–5167 (2010).
24. Lee, S. C. et al. G-Quadruplex in the NRF2 mRNA 5' untranslatable region regulates de Novo NRF2 protein translation under oxidative stress. *Mol. Cell. Biol.* **37(1)**, e00122-16. <https://doi.org/10.1128/MCB.00122-16> (2017).
25. Ma, Q. Role of Nrf2 in oxidative stress and toxicity. Annual Review of Pharmacology and Toxicology vol. **53** 401–426 Preprint at (2013). <https://doi.org/10.1146/annurev-pharmtox-011112-140320>
26. Almeida Lima, K. et al. Temozolamide Resistance in Glioblastoma by NRF2: Protecting the Evil. *Biomedicines* vol. **11** Preprint at. <https://doi.org/10.3390/biomedicines11041081> (2023).
27. Robertson, H., Dinkova-Kostova, A. T. & Hayes, J. D. Nrf2 and the ambiguous consequences of its activation during initiation and the subsequent stages of tumourigenesis. *Cancers (Basel.)* **12**, 1–48 (2020).
28. de la Roja, M., Chapman, E. & Zhang, D. Nrf2 and the Hallmarks of Cancer. *Cancer Cell* vol. **34** 21–43 Preprint at. <https://doi.org/10.1016/j.ccr.2018.03.022> (2018).
29. Adinolfi, S. et al. The KEAP1-NRF2 pathway: targets for therapy and role in cancer. *Redox Biology* Vol. <https://doi.org/10.1016/j.redox.2023.102726> (2023). 63 Preprint at.
30. Lin, T. Y., Cantley, L. C. & DeNicola, G. M. NRF2 rewires cellular metabolism to support the antioxidant Response. In A master regulator of oxidative Stress - The transcription factor Nrf2 (InTech, <https://doi.org/10.5772/65141> (2016).
31. Piska, K. et al. Comparative study on ABCB1-dependent efflux of anthracyclines and their metabolites: consequences for cancer resistance. *Xenobiotica* **53**, 507–514 (2023).
32. Engle, K. & Kumar, G. Cancer multidrug-resistance reversal by ABCB1 inhibition: A recent update. *Eur. J. Med. Chem.* **239**, Preprintat^{https://doi.org/10.1016/j.ejmech.2022114542} (2022).
33. Ji, L. et al. Nrf pathway regulates Multidrug-Resistance-Associated protein 1 in small cell lung cancer. *PLoS One* **8(5)**, e63404. <https://doi.org/10.1371/journal.pone.0063404> (2013).
34. Tang, Y. C. et al. How to deal with frenemy NRF2: Targeting NRF2 for chemoprevention and cancer therapy. *Journal of Food and Drug Analysis* vol. **31** 387–407 Preprint at. <https://doi.org/10.38212/2224-6614.3463> (2023).
35. Abd El-Aziz, Y. S., Spillane, A. J., Jansson, P. J. & Sahni, S. Role of ABCB1 in mediating chemoresistance of triple-negative breast cancers. *Biosci Rep* **41(2):BSR20204092**. doi:10.1042/BSR20204092 (2021).
36. Miodragović, D. et al. Iodide analogs of arsenoplatins—potential drug candidates for triple negative breast cancers. *Molecules* **26(17)**, 5421; <https://doi.org/10.3390/molecules26175421> (2021).
37. González-Ortiz, A. et al. eIF4A/PDCD4 Pathway, a Factor for Doxorubicin Chemoresistance in a Triple-Negative Breast Cancer Cell Model. *Cells* **11**, (2022).
38. Malekan, M. et al. VEGF/VEGFR axis and its signaling in melanoma: current knowledge toward therapeutic targeting agents and future perspectives. *Life Sci.* **345**, 122563 (2024).
39. Jiang, H. & Li, H. Prognostic values of tumoral MMP2 and MMP9 overexpression in breast cancer: a systematic review and meta-analysis. *BMC Cancer* **21(1)**, 149. <https://doi.org/10.1186/s12885-021-07860-2> (2021).

40. Blukacz, L. et al. Inhibition of the transmembrane transporter ABCB1 overcomes resistance to doxorubicin in patient-derived organoid models of HCC. *Hepatol Commun* **8**(5), e0437. <https://doi.org/10.1097/HC9.0000000000000437> (2024).
41. Tang, Z. et al. A web server for cancer and normal gene expression profiling and interactive analyses. *Nucleic Acids Res.* **45**, GEPIA, W98–W102 (2017).
42. Györffy, B. Integrated analysis of public datasets for the discovery and validation of survival-associated genes in solid tumors. *Innovation* **3**(3), 100625. <https://doi.org/10.1016/j.xinn.2024.100625> (2024).
43. Elefantova, K., Lakatos, B., Kubickova, J., Sulova, Z. & Breier, A. Detection of the mitochondrial membrane potential by the cationic dye JC-1 in l1210 cells with massive overexpression of the plasma membrane ABCB1 drug transporter. *Int J. Mol. Sci* **19**(7), 1985. <https://doi.org/10.3390/ijms19071985> (2018).
44. Muñoz-Ayala, A. et al. Tamoxifen metabolites treatment promotes ERα + transition to triple negative phenotype in vitro, effects of LDL in chemoresistance. *Biosci Rep* **44**(8), BSR20240444. <https://doi.org/10.1042/BSR20240444> (2024).
45. Harahap, Y., Ardiningsih, P., Winarti, A. C. & Purwanto, D. J. Analysis of the doxorubicin and doxorubicinol in the plasma of breast cancer patients for monitoring the toxicity of doxorubicin. *Drug Des. Devel Ther.* **14**, 3469–3475 (2020).
46. Hernández-Valencia, J. et al. Lapatinib-Resistant HER2 + Breast cancer cells are associated with dysregulation of MAPK and p70S6K/PCD4 pathways and calcium Management, influence of Cryptotanshinone. *Int J. Mol. Sci* **26**(8), 3763. <https://doi.org/10.3390/ijms26083763> (2025).
47. Mattioli, R. et al. Doxorubicin and other anthracyclines in cancers: Activity, chemoresistance and its overcoming. *Mol. Aspects Med.* **93**, 101205 (2023).
48. Won, K. A. & Spruck, C. Triple-negative breast cancer therapy: current and future perspectives. *Int. J. Oncol.* **57**, 1245–1261 (2020).
49. Paramanantham, A. et al. Doxorubicin-resistant Tnbc cells exhibit rapid growth with cancer stem cell-like properties and Emt phenotype, which can be transferred to parental cells through autocrine signaling. *Int J. Mol. Sci* **22**(22), 12438. <https://doi.org/10.3390/ijms222212438> (2021).
50. Mohammed, S. et al. Sublethal doxorubicin promotes migration and invasion of breast cancer cells: role of Src family non-receptor tyrosine kinases. *Breast Cancer Research* **23**(1), 76. <https://doi.org/10.1186/s13058-021-01452-5>, (2021).
51. Szklarczyk, D. et al. STRING v11: Protein-protein association networks with increased coverage, supporting functional discovery in genome-wide experimental datasets. *Nucleic Acids Res.* **47**, D607–D613 (2019).
52. Sadeghi, M. R. et al. Nrf2/P-glycoprotein axis is associated with clinicopathological characteristics in colorectal cancer. *Biomed. Pharmacotherapy* **104**, 458–464 (2018).
53. Sajadimajd, S. & Khazaei, M. Oxidative stress and cancer: the role of Nrf2. *Curr. Cancer Drug Targets* **18**, 538–557 (2017).
54. García-González, V. et al. Ceramide metabolism balance, a multifaceted factor in critical steps of breast cancer development. *International Journal of Molecular Sciences* vol. 19 Preprint at. <https://doi.org/10.3390/ijms19092527> (2018).
55. Fang, C. et al. EIF4E-eIF4G complex Inhibition synergistically enhances the effect of Sorafenib in hepatocellular carcinoma. *Anticancer Drugs* **32**, 822–828 (2021).
56. Tan, J., Ye, J., Song, M., Zhou, M. & Hu, Y. Ribavirin augments doxorubicin's efficacy in human hepatocellular carcinoma through inhibiting doxorubicin-induced eIF4E activation. *J Biochem. Mol. Toxicol* **32**(1), 10.1002/jbt.22007. <https://doi.org/10.1002/jbt.22007> (2018).
57. Park, J. et al. Using comparative proteomics to identify protein signatures in clear cell renal cell carcinoma. *Cancer Genomics Proteom.* **20**, 592–601 (2023).
58. dos Reis, S. B. et al. Mechanistic insights into the intracellular release of doxorubicin from pH-sensitive liposomes. *Biomedicine Pharmacotherapy* **134**, 110952. <https://doi.org/10.1016/j.biopha.2020.110952> (2021).
59. de Amorim, I. S. S. et al. APX2009 sensitizes hypoxic breast cancer cells to doxorubicin by increasing its accumulation and caspase-3/7-mediated apoptosis. *Breast Cancer Res. Treat.* <https://doi.org/10.1007/s10549-024-07512-6> (2024).
60. Leal-Orta, E., Ramirez-Ricardo, J., Cortes-Reynosa, P., Galindo-Hernandez, O. & Salazar, E. P. Role of PI3K/Akt on migration and invasion of MCF10A cells treated with extracellular vesicles from MDA-MB-231 cells stimulated with Linoleic acid. *J. Cell. Commun. Signal.* **13**, 235–244 (2019).
61. Oregel-Cortez, M. I. et al. Resistin induces migration and invasion in PC3 prostate cancer cells: role of extracellular vesicles. *Life* **13**(12), 2321. <https://doi.org/10.3390/life13122321> (2023).
62. Guevara-Olaya, L. et al. LDL Promotes Disorders in β-Cell Cholesterol Metabolism, Implications on Insulin Cellular Communication Mediated by EVs. *Metabolites* **12**(8), 754. <https://doi.org/10.3390/metabo12080754> (2022).
63. Lonsdale, J. et al. The Genotype-Tissue Expression (GTEx) project. *Nature Genetics* vol. 45 580–585 Preprint at. <https://doi.org/10.1038/ng.2653> (2013).
64. Ribeiro, J. V. et al. QwikMD - Integrative molecular dynamics toolkit for novices and experts. *Sci Rep* **6**, 26536. <https://doi.org/10.1038/srep26536> (2016).
65. Phillips, J. C. et al. Scalable molecular dynamics on CPU and GPU architectures with NAMD. *Journal Chem. Physics* **153**(4), 044130. <https://doi.org/10.1063/5.0014475>, (2020).
66. Kim, S. et al. CHARMM-GUI ligand reader and modeler for CHARMM force field generation of small molecules. *J. Comput. Chem.* **38**, 1879–1886 (2017).

Acknowledgements

The authors recognize the administrative support of Josue Villegas-Sandoval and Liliana García-Hernández. The authors recognize the antibody donations of Sta. Cruz Biotechnology Inc. (Antibodies anti-VEGF, anti-p-4E-BP1/2/3). The authors thank Dr. Nicolás Serafín-Higuera for the support in the flow cytometer experimentation.

Author contributions

Formal analysis, O.G.H, A.L.M and M.R.I.; Investigation, H.F.G, B.C.V, A.P.C., A.M.A. and V.G.G; Methodology, H.F.G, B.C.V, A.P.C., A.M.A. and V.G.G; Resources, V.G.G; Writing – original draft, H.F.G and V.G.G; All authors reviewed the manuscript.

Competing interests

The authors declare no competing interests.

Additional information

Supplementary Information The online version contains supplementary material available at <https://doi.org/10.1038/s41598-025-31313-6>.

Correspondence and requests for materials should be addressed to V.G.-G.

Reprints and permissions information is available at www.nature.com/reprints.

Publisher's note Springer Nature remains neutral with regard to jurisdictional claims in published maps and institutional affiliations.

Open Access This article is licensed under a Creative Commons Attribution-NonCommercial-NoDerivatives 4.0 International License, which permits any non-commercial use, sharing, distribution and reproduction in any medium or format, as long as you give appropriate credit to the original author(s) and the source, provide a link to the Creative Commons licence, and indicate if you modified the licensed material. You do not have permission under this licence to share adapted material derived from this article or parts of it. The images or other third party material in this article are included in the article's Creative Commons licence, unless indicated otherwise in a credit line to the material. If material is not included in the article's Creative Commons licence and your intended use is not permitted by statutory regulation or exceeds the permitted use, you will need to obtain permission directly from the copyright holder. To view a copy of this licence, visit <http://creativecommons.org/licenses/by-nc-nd/4.0/>.

© The Author(s) 2026